

Development of Cathode Material for The Rechargeable Al-Ion Battery

*A thesis submitted towards the partial fulfilment of BS-MS
programme by*

HEENA SUTHAR

20151162



Under the guidance of

Dr.-Ing. Jean-François Drillet



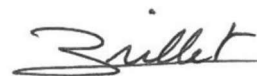
**Batteries & Fuel Cells, Technical Chemistry
60486 Frankfurt am Main, Germany**

CERTIFICATION

This is to certify that this dissertation entitled “**Development of cathode material for the rechargeable Al-ion battery**” towards the partial fulfilment of the BS-MS dual degree programme at the Indian Institute of Science Education and Research, Pune represents study/work carried out by “**Heena Suthar at DECHEMA Forschungsstitut (DFI)**” under the supervision of “**Dr.Ing. Jean-François Drillet, team leader Batteries and Fuel cells, Technical Chemistry department**” during the academic year **2019-2020**.



Signature of Student



Signature of Supervisor

Date: 29. March, 2020

Place: Frankfurt am Main

DECLARATION

I hereby declare that the matter embodied in the report entitled "Development of cathode material for the rechargeable Al-ion battery" are the results of the work carried out by me at the Department of Technical Chemistry, DECHEMA Forschungsinstitut, under the supervision of Dr. Ing. Jean-François Drillet and the same has not been submitted elsewhere for any other degree.



Signature of Student



Signature of Supervisor

Date: 29. March, 2020

Place: Frankfurt am Main

ACKNOWLEDGEMENTS

I would first like to express my deepest gratitude to Dr.-Ing.Jean-François Drillet, Team Leader Batteries and Fuel Cells at DECHEMA-Forschungsinstitut, Germany, who gave me such a great opportunity to work in his lab. Furthermore, I would like to thank Martin Eckert for his supervision, advice, teaching, for directing me and improving me throughout my ten months journey in DECHEMA. I am grateful for having him as my advisor. He gave me the freedom to implement new ideas and was patient in explaining concepts of research and writing. I am indebted to him for his astonishing and master guidance during my project work.

I would like to pay my special regards to the director of IISER-PUNE Prof. Jayant B. Udgaonkar for giving a chance to completing this exploration work. My exceptional much gratitude goes to Dr. Muhammed Musthafa O.T. at IISER Pune for being my TAC member, and for his guidance and support.

The amount of lab space and facilities at DECHEMA-Forschungsinstitut which I have been permitted to use gratefully acknowledged. In this regard I would like to thank Nicky Bogolowski, Dr. Sakthivel Mariappan, Gerald Schmidt, Melanie Thalheimer, Martin Eckert for introduce me characterization techniques. I thank whole technical chemistry group people at DECHEMA Forschungsinstitut for their support in the laboratory. I gladly acknowledge my friends, Swati Choudhary, Nupur Sontakkey, Bhawana M. for their constant support.

HEENA SUTHAR

CONTENTS

LIST OF FIGURES

LIST OF TABLES

ABSTRACT

1. INTRODUCTION	12
1.1. Li-Ion Batteries (LIB).....	12
1.1.1. Working principle of Li-ion battery and challenges	13
1.2. Al-Ion Batteries (AIB).....	14
1.2.1. Working principle of rechargeable Al-ion battery.....	15
1.3. Carbon Xerogels: a cathode material in Al ion battery.....	16
1.4. Motivation and Aim.....	19
2. MATERIALS AND METHODS.....	20
2.1. Experiment Section 1: Synthesis of C_{XG}.....	20
2.1.1. List of chemicals.....	20
2.1.2. Synthesis procedure of C_{XG}.....	20
2.1.2.1. Resorcinol-formaldehyde gel formation.....	21
2.1.2.2. Gel drying.....	24
2.1.2.3. Pyrolysis	25
2.2. Experiment Section 2: Electrochemical experiments (Al/C_{XG})	26
2.2.1. Ink preparation.....	26
2.2.2. Spray coating.....	27
2.2.3. Electrochemical measurement setup.....	29
2.2.4. Galvanostatic charge/discharge measurements of AIB.....	30
2.2.5. Cyclic voltammetry (CV).....	31
2.3. Experiment Section 2: Characterization techniques for C_{XG}	31
2.3.1. Thermogravimetric analysis (TGA).....	31
2.3.2. Scanning electron microscope (SEM).....	33
2.3.3. X-ray diffraction (XRD).....	34
2.3.4. Raman spectroscopy	36
2.3.5. Brunauer-Emmett-Teller (BET).....	37
2.4. Electrochemical Characterization Techniques.....	38
2.4.1. Cyclic voltammetry (CV)	38

2.4.2. Galvanostatic charge-discharge (GCD).....	39
3. RESULTS AND DISCUSSION	40
3.1. Carbon Xerogel Synthesis.....	40
3.2. Thermal Degradation of Xerogel during Carbonization in TGA apparatus.....	41
3.3. Surface Characterization of C_{XG}	42
3.4. Effect of Resorcinol/Catalyst ratio (R/C) on Porous Structure.....	44
3.5. Pore Size Distribution	45
3.6. Scanning Electron Microscopy (SEM) of C_{XG}	46
3.7. Electrochemical Performance of AIB with C_{XG}	48
3.7.1. Half-cell measurements.....	48
3.7.2. Galvanostatic charge/discharge	49
3.7.2.1. Discharge capacity evaluation of AIB with C_{XG} R/C ₅₀	49
3.7.2.2. Discharge capacity evaluation of AIB with R/C ₅₀₀ , R/C ₁₀₀₀ and R/C ₁₅₀₀	50
3.7.2.3. Discharge capacity evaluation of R/C ₂₀₀₀ and R/C ₂₅₀₀	53
3.7.2.4. Discharge capacity evaluation of Natural Graphite (NG).....	54
3.8. Post-Mortem Study of C_{XG} Cathode After Electrochemical Tests.....	56
4. CONCLUSION	60
5. REFERENCES.....	62

LIST OF FIGURES

Figure 1: Schematic diagram of working principle of rechargeable Li-ion battery.....	13
Figure 2: Schematic diagram of Al/graphite cell during discharging.....	15
Figure 3: Reaction mechanism of sol-gel polymerization.....	17
Figure 4: Measured and calculated pH value of catalyst Na_2CO_3 and reaction solution.....	23
Figure 5: Xerogel carbonization.....	25
Figure 6: Ball miller	27
Figure 7: Ultra-Turrax machine.....	27
Figure 8: Spray coating of C_{XG} ink on Toray carbon paper.....	27
Figure 9: Electrode cutting	28
Figure 10: A) Glove box B) Schematic diagram of ELcell.....	29
Figure 11: Galvanostatic charge-discharge measurement setup.....	30
Figure 12: Half cell CV measurement setup.....	31
Figure 13 Simultaneous Thermogravimetry-Differential Scanning Calorimetry.....	32
Figure 14: A) Column structure of SEM B) SEM analyzer.....	33
Figure 15: Schematic representation of Bragg's Law.....	34
Figure 16: XRD analyser for powder C_{XG} sample.....	35
Figure 17: Schematic diagram of Rayleigh scattering, Raman stokes and anti-stokes scatterings.....	36
Figure 18: Confocal RAMAN microscope.....	37
Figure 19: Adsorption isotherm types defined by Brunauer.....	38
Figure 20: Cyclic Voltammetry.....	39
Figure 21: Xerogels as suspension, powder form and after carbonization.....	40
Figure 22: TGA curve for R/C ₅₀ C_{XG} in Argon atmosphere	41
Figure 23: Raman spectra of all prepared C_{XGs} with PG and NG.....	42

Figure 24: XRD diffraction pattern of carbon C _{XG} with NG as ref.....	44
Figure 25: Isotherm curves of R/C ₅₀₀ and R/C ₂₅₀₀ C _{XG}	45
Figure 26: Pore size distribution.....	46
Figure 27: SEM images of RF gels.....	47
Figure 28: CV curves of C _{XG} and Al deposition/dissolution.....	48
Figure 29: Discharge capacity evaluation of R/C ₅₀	49
Figure 30: Discharge capacity evaluation of R/C ₅₀₀	51
Figure 31: Discharge capacity evaluation of R/C ₁₀₀₀	52
Figure 32: Discharge capacity evaluation of R/C ₁₅₀₀	52
Figure 33: Discharge capacity evaluation of R/C ₂₀₀₀	53
Figure 34: Discharge capacity evaluation of R/C ₂₅₀₀	54
Figure 35: Discharge capacity evaluation of NG.....	55
Figure 36: Compared galvanostatic charge/discharge curve of C _{XG} in AIB.....	56
Figure 37: Post-mortem study of C _{XGs}	58

LIST OF TABLES

Table 1: Composition of the starting precursor solutions.....	22
Table 2: Measured and calculated pH of cat. and reaction solution.....	24
Table 3: Active material (C_{xG}) mass with respect to their corresponding R/C value.....	28
Table 4: I_D/I_G values with respect to their R/C values.....	43
Table 5: Pore texture properties of R/C ₅₀₀ and R/C ₂₅₀₀	46
Table 6: Discharge capacity and coulombic efficiency comparison of R/C ₅₀₀ , R/C ₁₀₀₀ and R/C ₁₅₀₀	50
Table 7: Capacity comparison of C_{xG} R/C ₅₀₀ , R/C ₁₀₀₀ and R/C ₁₅₀₀ with NG.....	56
Table 8: I_D/I_G values comparison between pristine electrode and treated electrode.....	59
Table 9: Summary of discharge capacity and coulombic efficiency.....	60

ABSTRACT

Many research activities focus on emergent energy storage technologies such as Na-ion, Zn-ion and Al-ion as alternative systems to established ones like lead acid, NiMH and Li-ion batteries. Function principle of an Al-ion cell in AlCl_3 containing electrolyte is more similar to that of a Li-metal one where Al dissolution/deposition occurs from/on Al foil during cell charge/discharge step leading to AlCl_4^- ion deintercalation/intercalation from the graphitic carbon counter electrode. The state-of-the-art of Al-ion cell faces several challenges e.g. dendrites growth at the metal electrode and delamination of graphitic layers in pyrolytic graphite due to repetitive intercalation/deintercalation of large AlCl_4^- ions at positive electrode. In that context, search for more stable intercalation materials is of great importance for sustainable Al-ion battery development. In this work different resorcinol-formaldehyde-based carbon xerogels were successfully synthesized by varying resorcinol/catalyst ratio and their electrochemical performance as positive electrode material was evaluated in Al ion battery system.

Carbon xerogels (C_{XG}) were synthesized by polycondensation of resorcinol (R) with formaldehyde (F) in presence of sodium carbonate as catalyst (C). In order to find out optimal Resorcinol to catalyst ratio (R/C), fourteen different carbon xerogels (C_{XGs}) samples ($50 < \text{R/C} < 20.000$) were produced. The synthesis mainly involved addition and condensation reaction between resorcinol and formaldehyde in presence of Na_2CO_3 followed by vacuum drying at 0.2 mbar and pyrolysis at 800°C . Mass loss behavior of C_{XG} with temperature is evaluate by Thermogravimetric analysis (TGA). The presence of disorder mode of C (sp^3) and tangential mode of C (sp^2) carbons was evidenced by emergence of both D band (1352 cm^{-1}) and G band (1598 cm^{-1}) in Raman spectra of all C_{XG} samples. All C_{XG} materials was found to be amorphous by X-ray diffraction pattern. and the surface morphology was demonstrated by Scanning Electron Microscopy (SEM). Further, the electrochemical performance of selected C_{XGs} (R/C₅₀, 500, 1000, 1500, 2000 & 2500) was studied in Al ion battery system on cathode side. With specific surface area of $720 \text{ m}^2\text{g}^{-1}$, Al-ion cell with R/C₅₀₀ C_{XG} cathode enabled a gravimetric discharge capacity of 88 mAhg^{-1} at 0.5 mA current with 85% coulombic efficiency. In addition, cells with R/C₁₀₀₀ and R/C₁₅₀₀ displayed gravimetric discharge capacity of 101 mAhg^{-1} and 96 mAhg^{-1} with 77% and 84% coulombic efficiency, respectively. To summarize, best results in

terms of capacity were yielded by Al-ion cells with carbon xerogels R/C₅₀₀, 1000 & 1500 ratios which comparable to that obtained with natural graphite (NG).

Equipment's and Instruments

a) Synthesis

Instrument	Manufacturer
Vacuum Drying Oven	Thermo scientific Vacuum oven VT6025

b) Material (C_{XG}) Characterization

Instruments	Manufacturer
RAMAN Spectroscopy	Reinshaw inVia Raman Microscope
X-Ray Diffraction	Bruker D8 Advance
Scanning Electron Microscopy	FlexSEM 1000 II
Thermo Gravimetric Analysis	NETZSCH Jupiter STH 449
Brunauer-Emmett-Teller	Quantichrome Autosorb iQ ₃

c) Electrode coating & electrochemical Characterization

Instruments/Equipments	Manufacturer	Type
Ball Mill	Retech	PM 100
Toray Paper	QuinTech	TGP-H-060
Ultra-Turrax	IKA	T25 digital
Glove Box	MBRAUN	UNIlab plus Eco
Electrochemical Test-Cells	EL-Cell	EL-Cell AIR
Reference Electrode	ChemPur	Aluminium
Separator	EL-Cell	Glass fiber
Potentiostat	BioLogic	BCS810

1. INTRODUCTION

In the perspective of replacing the conventional fossil fuel-based energy sources, there is an increasing demand of reliable and clean renewable energy sources. Currently, the world is still drawing nearly 80% of its energy demand from the fossil fuels. Since the problems such as environmental pollution, global warming and ozone depletion is becoming worse day by day, it's a need of the hour to switch to sustainable, affordable and more environmentally friendly energy sources. Batteries, supercapacitors and fuel cells are electrochemical power sources that enable renewable energy generation to be stored until required. Batteries and supercapacitors store electrochemical energy while fuel cells are an ideal primary energy conversion device.

Battery converts stored chemical energy into electrical energy on demand via redox reaction at anode and cathode¹. Batteries are categorized into two types' primary and secondary batteries. Primary batteries are non-rechargeable battery system because the chemical reaction is not reversible. Due to lack of active chemical species, these types of battery die after one-time use. Whereas in secondary batteries the chemical reaction is reversible hence they are rechargeable. Nickel-cadmium (Ni-Cd) battery, Lead acid battery, Nickel-metal hydride battery (Ni-MH), Li ion, and Al-ion batteries are some secondary batteries. Ni-Cd was the first small sealed rechargeable battery but after the development of Li-ion batteries, the use of Ni-MH and Ni-Cd battery became limited because Li-ion battery comprises high gravimetric and volumetric density than Ni-MH and Ni-Cd. Now a day's Li-ion is the fastest growing and most promising battery chemistry with significantly higher energy density and lighter weight, mostly used for portable electronics and electric vehicles.

1.1. Lithium-Ion Batteries (LIB)²

From a last few decades Li ion battery is a dominant rechargeable battery in market. Li-ion batteries are the powerhouse for the digital electronic revolution. It is the most popular type of rechargeable battery for consumer electronics like mobile-phones, and laptops, computers. The gravimetric energy density of Li ion battery is 3.86 Ah/g and volumetric energy density of 2.06 Ahcm⁻³. Li-ion batteries are better than any other rechargeable battery system (lead acid, and Nickel cadmium batteries) in following criteria-

1. It contains comparatively low level of toxic metals than Pb-acid and Ni-Cd batteries
2. Li and carbon electrodes are used in Li-ion battery which are lightweight their own, make the battery compact, lightweight and also design flexible
3. These batteries are compact battery system that stores tremendous amount of energy in small size (high energy density). A typical Li-ion battery has cell voltage of 3.6V which means a designer is required to use three series connected Ni-Cd or Ni-MH cells to equal the voltage of a single Li-ion cell.
4. It has very low self-discharge rate (<5% per month) than Ni based battery (20-30% per month) at 20°C.

1.1.1. Working principle of Li ion battery and challenges-

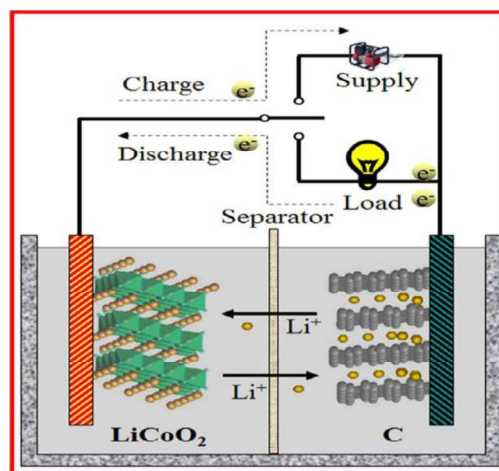
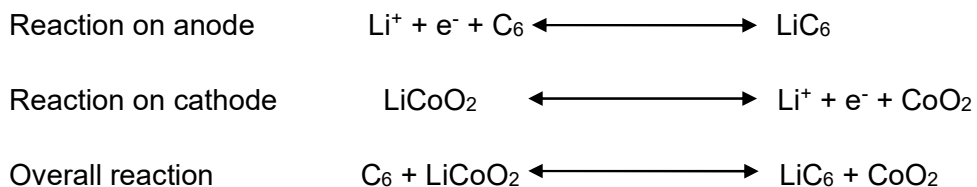


Figure 1: schematic diagram of working principle of rechargeable Li-ion battery

In typical Li-ion batteries carbon is used as anode material and Li ion transition compounds such as LiCoO_2 , LiMn_2O_4 , LiNiO_2 , LiFePO_4 are used as cathode material. In between of anode and cathode an electrolyte, containing Li ions is present. A separator isolates anode and cathode. During charging process electrons move from cathode to anode through external circuit. At the same time, Li ions also move in same direction via electrolyte. The opposite occurs during discharging. The movement of Li ions between anode and cathode is also known as “shuttle chair” mechanism. The anode and cathode reactions are given below-



Challenges with Li-ion battery system-

1. These batteries are way more expensive than Ni-Cd batteries
2. Limited sources of Li and Co
3. Since, the discharge curve for an ideal battery is flat but Li-ion battery shows declining discharge curve
4. Since these batteries contain a large amount of energy in a small package with high internal resistance. In this case if the cell is shorted accidentally, the temperature could raise a lot and it may result an explosion.

1.2. Al-Ion Batteries (AIB)

Among various battery technologies Al ion battery, has gained attention due to high abundance, low cost, light weight, and corrosion resistance of Al metal. Al-ion batteries, with three-electron transfer, could achieve three times higher energy density than that of Li-ion batteries, offers the possibility to replace Li ion batteries in near future from electronic portable devices.

Gravimetric energy density of Al and Li is quite comparable ($\text{Al} = 2.98 \text{ Ahg}^{-1}$ and $\text{Li} = 3.82 \text{ Ahg}^{-1}$). However, the volumetric energy density of Al is about four times higher than Li ($\text{Al} = 8.04 \text{ Ahcm}^{-3}$ and $\text{Li} = 2.06 \text{ Ahcm}^{-3}$). It means Al ion batteries can contain energy four times higher in comparison to its volume than Li ion batteries. However, Al ion batteries are not all the way perfect; there are a couple of limitations also associated to them, for example, use of expensive ionic liquids, low working voltage (1.8 V), intercalation of large AlCl_4^- anion ($\sim 5.28 \text{ \AA}$), low capacity and poor cycling stability. The major problem with this system is Al deposition. Since Al has very negative standard potential (-1.66V vs SHE), it is not possible to deposit Al in aqueous media.

In a typical Al ion battery system non-aqueous media is used as electrolyte. Inorganic molten salts, organic molten salts (ionic liquid) and molecular organic solvents are three categories of non-aqueous solutions that have been developed for Al ion battery as an electrolyte. The most widely used electrolyte is ionic liquid

because of its huge advantages over inorganic molten salts and molecular organic solvent. Ionic liquid is a salt in liquid state made up of ions and short-lived ion pairs, hence possess specific conductivity in mScm^{-1} . Ionic liquid has low melting point, high thermal and chemical stability and low vapour pressure. 1-Ethyl-3-methyl-imidazolium chloride (EMImCl/ AlCl_3), 1-Butyl-3-methyl-imidazolium chloride, 1-Ethyl-3-methyl-imidazoliumbromide are few examples of ionic liquid used in Al ion battery³⁻⁵.

1.2.1. Working principle of rechargeable Al ion battery-

An Al ion battery (AIB) system is composed of an Al foil anode, a graphite cathode, and an ionic liquid electrolyte (e.g.- EMImCl / AlCl_3). The mobile AlCl_4^- ions in the electrolyte, bridge the anode and cathode and electrochemically react with Al and carbon during charging and discharging process as shown in figure 2

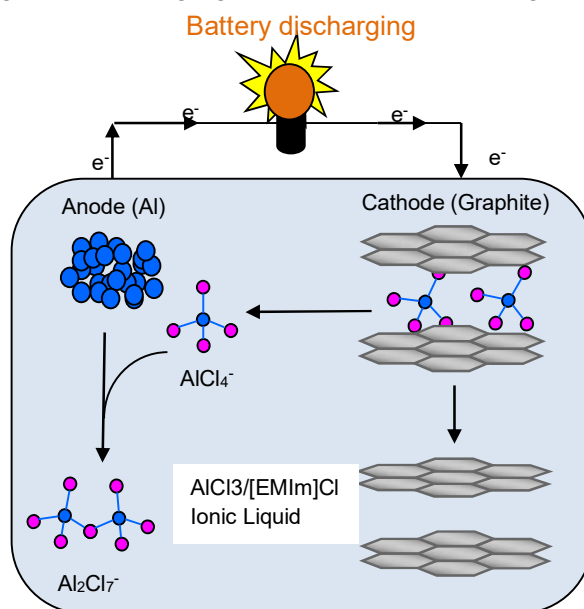
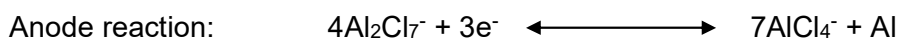


Figure 2: Schematic diagram of Al/graphite cell during discharging

Reactions during charging and discharging:



During discharging process, intercalated AlCl_4^- ions are extracted from carbon (graphite) and move towards anode (Al). When AlCl_4^- ions approach to anode, they react with metallic Al and produce Al_2Cl_7^- and three electrons. These electrons then

move from anode to cathode. Both anodic and cathodic reactions are highly reversible during charging/discharging process, forming an entire recyclable secondary battery system.

An AIB with Al foil on anode and graphite on cathode can achieve specific capacity close to 70 mAhg^{-1} with discharge voltage plateaus in the range of 2.25 V - 2 V and 1.9 V-1.5 V. Although these plateaus are lower than the voltage of LIB (3.5 V - 4V), but comparable with commercial lead acid and Ni-metal hydride (Ni-MH) batteries. One of the most distinctive feature of Al ion battery system is the ability to charge and discharge very fast. Moreover, it has to be noticed that voltage and specific capacity of AIB system could be further advanced via exploring new cathode material and electrolyte. Numerous research groups all around the globe are facing the challenge to find out suitable cathode material and electrolyte to increase capacity and energy density of Al ion battery^{6,7}.

1.3. Carbon Xerogels: a cathode material in Al-ion battery

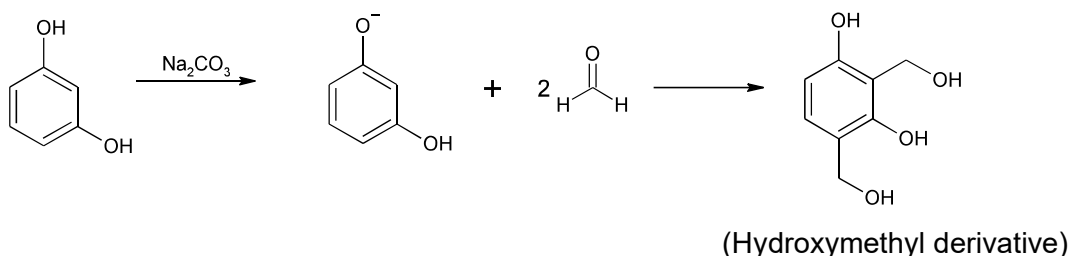
Carbon gels are synthetic polymeric carbon materials known for their tuneable porosity, surface area and morphology. Aerogels, cryogels and xerogels are three organic gels that are synthesized by sol-gel polycondensation method. The difference among these three organic gels is the drying procedure. Aerogels are produced by CO₂ supercritical drying after solvent exchange (by acetone or ethanol). On the other hand, cryogels are obtained by freeze drying in which solvent is removed by sublimation under low pressure. However, these two drying procedures are expensive and difficult to handle. Surprisingly carbon s are acquired by simple vacuum drying and pyrolysis of aqueous resorcinol-formaldehyde gel, gives very porous carbon material⁸.

- **Mechanism of carbon xerogel (C_{XG}) synthesis**

Before 1987 hydrolysis and condensation of metal alkoxides was the traditional synthetic route for inorganic aerogels synthesis. The first organic aerogel synthesis route was given by Pekala in 1989 by sol-gel polycondensation reaction with resorcinol and formaldehyde in the presence of catalyst, has become the most widely used route to synthesize organic gels in today's date⁹. In order to synthesize C_{XG}, a number of precursors can be used such as phenol, cresol, cellulose or tannins. In this thesis, resorcinol is used as precursor. Sol-gel polycondensation

reaction takes place in two steps, formation of colloidal solution of monomers followed by formation of gel. Addition reaction and condensation reaction are two chemical reaction involved in gel formation. An aqueous medium and a catalyst (Na_2CO_3 , KOH , NaOH) are required for the reaction to be done. The reaction mechanism is explained in figure 3 which includes two steps. First, formation of resorcinol anions by proton abstraction with base catalyst occurs. Addition of formaldehyde gives rise to hydroxymethyl derivatives.

Addition Reaction



Second, condensation of hydroxymethyl derivatives with proton catalyst and growth of cluster as follows:

Condensation Reaction

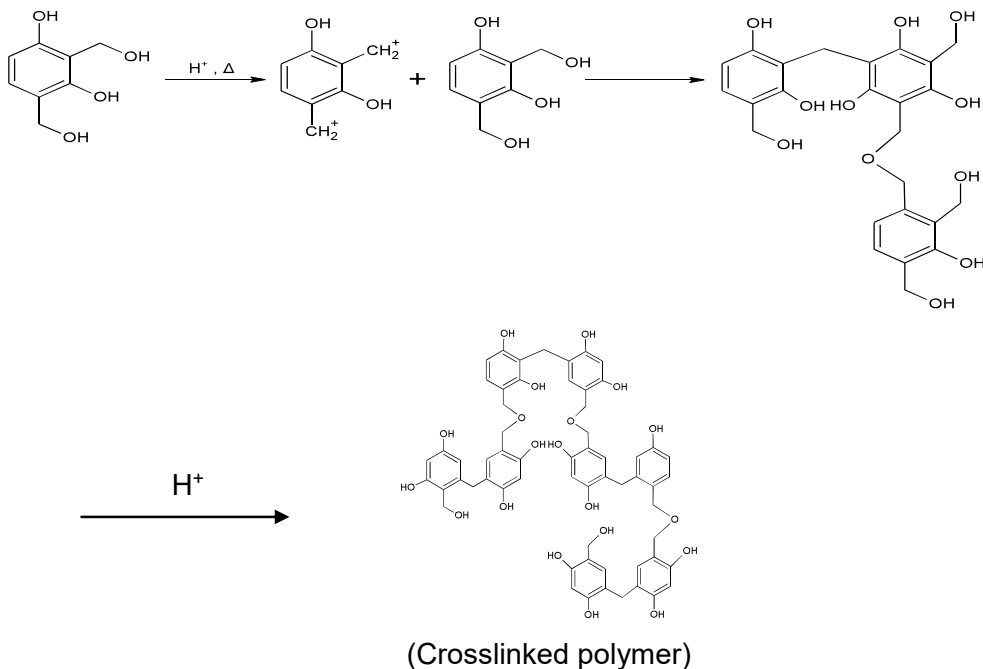


Figure 3: Reaction mechanisms of the sol-gel polymerization of resorcinol with formaldehyde¹⁰

First the monomers are dissolved in reaction media, the polycondensation reaction starts and a suspension of colloidal solid particles is formed (sol). These particles are called nodules of polymeric material. These nodules grow and interconnect in 3D fashion (formation of gel) and the liquid starts to densify and forms a polymeric cross-linked solid structure called organic gel. The pores (micro, meso and/or macropores) are formed during the polymerization process and also during drying step when the excess solvent, present in the interspaces between the nodules, is drawn off. By contrast to aerogels and cryogels that are obtained by supercritical and cryogenic drying, respectively, C_{XG} formation undergoes subcritical drying of the gel for solvent elimination. Perhaps the most relevant property of carbon C_{XGs} is that their meso porosity and macro porosity can be tailored during the synthesis of the organic xerogels by selecting the appropriate precursor solution composition and synthesis conditions¹⁰.

To achieve carbon structures from organic gels they have to be carbonized at high temperatures >800 °C to ensure full carbonization. During carbonization, volatile molecules such as H_2O , CO , and CO_2 are released at temperature >400 °C and leaves micropores in the resulted C_{XGs} . Higher pyrolysis temperatures than 900 °C, however, can lead to collapse of pore network.

C_{XGs} are thermally stable materials that possess a high number of sp^2 hybridized carbon. They are highly porous material with high electrical conductivity (110 Sm^{-1}) which makes them ideal materials to use as electrodes in energy storage devices. One of the most peculiar properties of C_{XG} is that their porosity can be tuned according to the synthesis and processing conditions. Type and amount of solvent, pH, concentration of reactants, type of catalyst, and the concentration of catalyst, reaction time, reaction temperature and drying process (e.g. temperature and vacuum) of synthesis are some variables that control the porosity of C_{XGs} ¹¹.

1.4. Motivation and Aim

Aluminium is the most abundant metal in earth crust. Al based redox reaction involved three electron transfer during electrochemical charge/discharge reaction that offers potential to compete with Li-ion battery. In 2015, Dai's group presented an ultrafast charging Al-ion battery by using pyrolytic graphite (PG) sheet with covalent-bonding of graphene layers or three dimensional (3D) graphitic foam as cathode⁷. While PG is prone to delamination during intercalation/deintercalation of large AlCl_4^- anion, graphite foam necessitates use of e.g. Ni foam template that may corrode in contact with $\text{EMImCl}/\text{AlCl}_3$, capacity of nature graphite shrinks at high current density¹² due to mass transport limitation within large graphite particle. Therefore, a three-dimensional carbon material structure with define mesoporous structure should permit more efficient anion (AlCl_4^-) intercalation/deintercalation necessary for higher battery performance and longevity. In this work, carbon C_{XG} was investigated as potential cathode material because of its highly tunable pore distribution, high surface area, easy synthesis procedure and cheap reaction substances. Three dimensional structures of C_{XGs} are believed to better handle the volume expansion of the active material in the cathode during cycling compared to two-dimensional natural graphite (NG).

The main objectives to be obtained are as follows-

- Development of cathode material and electrochemically testing of Al alloy as anode for the rechargeable Al ion battery
- Synthesize resorcinol-formaldehyde based carbon C_{XGs} by sol-gel polycondensation method by varying catalyst (Na_2CO_3) amount
- Study the influence of catalyst ratio on particle size (SEM), pore size distribution and surface area (isotherm, BET), thermal stability (TGA) and graphitization level (XRD, Raman) of carbon C_{XGs}
- Electrochemical testing (galvanostatic charge-discharge, cyclic voltammetry) of carbon xerogels C_{XG} in EL cells and comparison with natural graphite.

2. MATERIALS AND METHODS

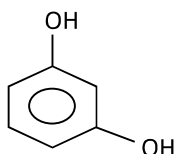
2.1. Experimental Section 1: Synthesis of C_{XG}s

2.1.1. List of chemicals:

a) Resorcinol

Manufacturer/ source: Sigma Aldrich

Structure:



b) 37% Formaldehyde (HCHO) stabilized with 10% methanol

Manufacturer/ source: Sigma Aldrich

Addition reaction between resorcinol and formaldehyde helps to make branched and interconnected structure that strengthens the gel.

c) Sodium carbonate (Na₂CO₃)

Manufacturer/ source: Sigma Aldrich

The reaction speed depends on the amount of sodium carbonate. It deprotonates the resorcinol and generates resorcinol anions. Its primary role is to increase the pH of reaction media

2.1.2. Synthesis procedure of C_{XG}

Carbon xerogels were produced by resorcinol-formaldehyde polycondensation reaction in aqueous media with the help of a catalyst, followed by drying and pyrolysis. The final texture of C_{XG}s depends on three variables, which are resorcinol/formaldehyde molar ratio (R/F), dilution ratio (D), and resorcinol/sodium carbonate molar ratio (R/C).

In this thesis only R/C ratio was varied and other parameters were kept constant. Resorcinol/formaldehyde gel formation, gel drying and pyrolysis are three steps in order to produce C_{XGs} which are discussed below-

2.1.2.1. Resorcinol-formaldehyde gel formation

- Xerogels were prepared by polycondensation of resorcinol (R), solubilized in water, with formaldehyde (F), in the presence of sodium carbonate (C)
- Fourteen different resorcinol-formaldehyde solutions were prepared with various R/C ratios: R/C₅₀, R/C₅₀₀, R/C₇₅₀, R/C₁₀₀₀, R/C₁₅₀₀, R/C₂₀₀₀, R/C₂₅₀₀, R/C₃₀₀₀, R/C₃₅₀₀, R/C₄₀₀₀, R/C₄₅₀₀, R/C₅₀₀₀, R/C₁₀₀₀₀, R/C₂₀₀₀₀
- Resorcinol - formaldehyde molar ratio was fixed at 0.5 (stoichiometric ratio)
- Dilution ratio (D) was fixed at 5.7, dilution ratio is the molar ratio of solvent and resorcinol and formaldehyde combination (solvent / R+F)
- 0.1 M Na₂CO₃ solution was prepared in a 100 ml volumetric flask and it was diluted in fourteen different volumetric flask (50ml) according to R/C ratios with ultra-pure water (18.2 MΩ)
- 1.95 ml of diluted Na₂CO₃ was taken from each flask and mixed with 1 g resorcinol in fourteen different vials. For thoroughly mixing of resorcinol, a 15 min sonication bath was provided
- After sonification 1.35 ml formaldehyde (37 wt.% in water + 10% methanol) was poured in each vial and mixed properly by shaking
- Table 1 shows the composition of the starting solutions
- All the solutions were then placed in a water bath at 60°C for 72 h
- The obtained product was resorcinol-formaldehyde gel.

Table 1: Composition of the starting precursor solutions

R/C	Dilution ratio (D)	Resorcinol g	Formaldehyde ml	0.1M Sodium carbonate μl
50	5.7	1.00	1.35	46530
500	5.7	1.00	1.35	4650
750	5.7	1.00	1.35	3100
1000	5.7	1.00	1.35	2330
1500	5.7	1.00	1.35	1550
2000	5.7	1.00	1.35	1160
2500	5.7	1.00	1.35	930
3000	5.7	1.00	1.35	780
3500	5.7	1.00	1.35	660
4000	5.7	1.00	1.35	580
4500	5.7	1.00	1.35	520
5000	5.7	1.00	1.35	470
10000	5.7	1.00	1.35	230
20000	5.7	1.00	1.35	120

The mechanism of resorcinol-formaldehyde reaction in the presence of sodium carbonate is presented in figure 3 in section 1.3.

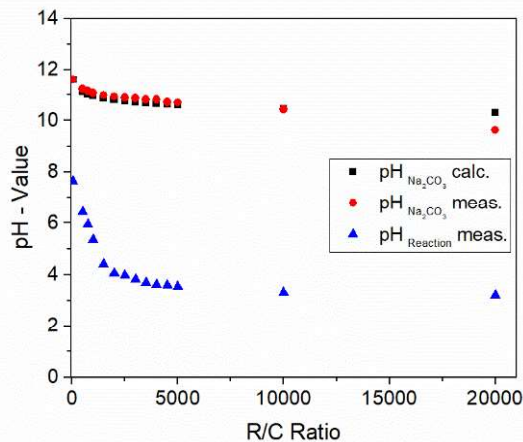


Figure 4: Measured and calculated pH value of catalyst Na_2CO_3 and reaction solution (catalyst + resorcin + formaldehyde)

As shown in figure 4, the measured pH value depends strongly on the concentration of added catalyst Na_2CO_3 . The pH values vary from 7.65 at R/C_{50} till 4.06 at R/C_{2000} . From literature it is known that beyond a certain pH value the reaction of resorcinol and formaldehyde leads to mostly microporous or even nonporous structures ($\text{pH} > 6.5$) or mostly macroporous structures ($\text{pH} < 5.2$)¹³.

An overview of measured pH values is shown in table 2.

The reason can be explained by the degree of deprotonation of the resorcin in the first polymerization step. The pK_a value of resorcin is around 9.48 for the first (-ortho) deprotonation step and around 12.08 for the 2nd step (full deprotonation).

These values can be read as follows: At pH 9.48 around 50 % of the ortho position is deprotonated. At pH 12.08 the ortho position is completely deprotonated while additionally the meta position is 50 % deprotonated. These mechanisms are important to understand the polymerization rate of resorcinol and formaldehyde.

Table 2: Measured and calculated pH of catalyst and reaction solution

R/C Ratio	pH Na ₂ CO ₃ calc.	pH Na ₂ CO ₃ meas.	pH Reaction solution
50	11.61	11.60	7.65
500	11.11	11.22	6.42
750	11.02	11.15	5.94
1000	10.96	11.08	5.35
1500	10.87	10.98	4.41
2000	10.81	10.93	4.06
2500	10.76	10.89	3.98
3000	10.72	10.87	3.82
3500	10.69	10.82	3.69
4000	10.66	10.81	3.63
4500	10.63	10.72	3.59
5000	10.61	10.70	3.54
10000	10.46	10.43	3.32
20000	10.31	9.63	3.21

In RC₅₀ the initial pH value was measured to be 11.61. The inside dissolved resorcin can be expected to be completely deprotonated. Therefore, the following nucleophilic attack on formaldehyde is very fast which results in a more or less unordered reaction product. As a result, the obtained polymer is mostly nonporous or contains very small pores.

The lower the deprotonation degree (lower pH value), the slower the polymerization rate and the greater the probability to form a kind of a porous system.

The measured pH values of R/C values >2500 are more or less comparable (pH ~3.98 – 3.21). Those mixtures should contain mostly mesopores or even macropores. A too high concentration of macropores can induce poor mechanical stability of carbon structure as described by Job et. al¹³.

2.1.2.2. Gel drying

Carbon gels obtained from above step were dried at 125 °C under vacuum with pressure ~0.2mbar for 24 h.

2.1.2.3. Pyrolysis

Dried xerogels were carbonized under N₂ atmosphere in a tubular oven (figure 5A). The temperature was raised from room temperature to 400°C and maintained at 400°C for two hours, followed by a temperature rising from 400°C to 800°C and held constant for two hours again. Both heating ramps (room temperature to 400°C and 400°C to 800°C) were set to 5°C/min. The schematic diagram of temperature gradient is shown in figure 5B

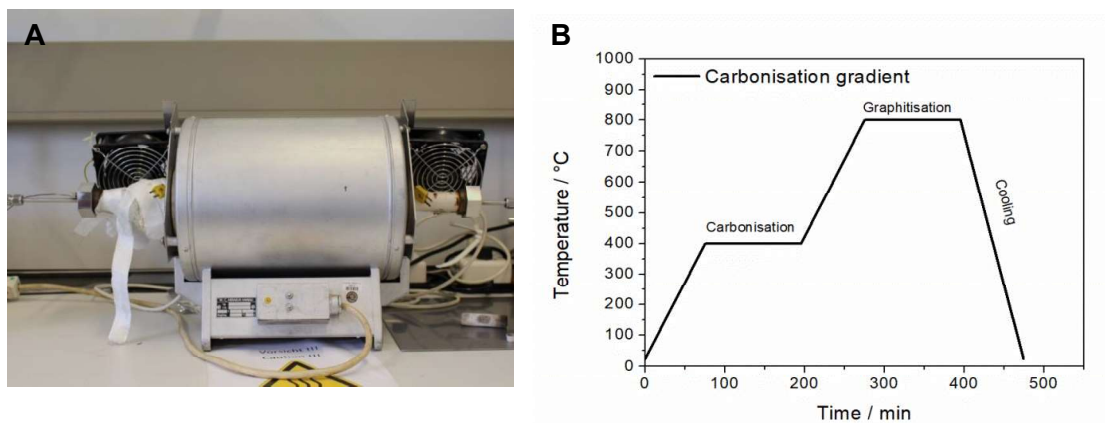
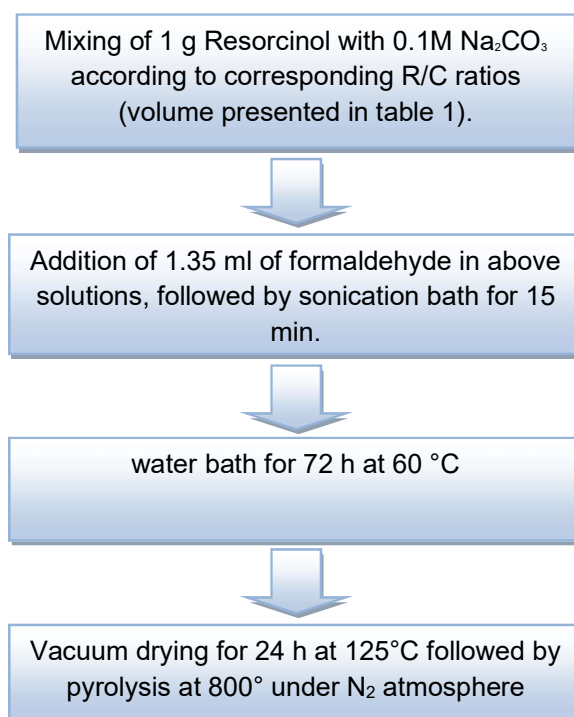


Figure 5: C_{xG} Carbonization A) tubular oven B) Scheme of temperature gradient

The schematic diagram of synthesis method is presented below:



2.2. Experimental Section 2: Electrochemical experiments (Al / C_{XG})

Chemicals	Manufacturer
2-propanol	Carl Roth
Polytetrafluoroethylene (PTFE)	ElectroChem, Inc.
Toray carbon paper (TP-H-060)	QuinTech

2.2.1. Ink preparation

In the process of ink preparation, ball milling is a crucial step to pulverize, mix and make the sample homogeneous. In addition to highest degree of fineness, colloidal grinding, and mechanical alloying can also be achieved with ball mill instrument. Grinding can be carried out under either wet or dry conditions. The advantage of wet grinding is that powder doesn't stick on container wall and grinding process becomes homogeneous, increased capacity. Additionally, there is no dust formation. In this work, ball milling was carried out with RETSCH planetary ball mill PM 100 (figure 6). Before ink preparation, carbon xerogels (C_{XG}) with R/C₅₀, R/C₅₀₀, R/C₁₀₀₀, R/C₁₅₀₀, R/C₂₀₀₀, and R/C₂₅₀₀ ratios were ball milled. Wet ball milling was used in this work in which powder of C_{XG} was mixed with few drops of ethanol and was ball milled for 2h at 400 rps.

The ink was composed of 90 % active material (C_{XG}) and 10% polytetrafluoroethylene (PTFE) in a solution of 3:7 (volume %) water and 2-propanol. The C_{XG} loading on Toray paper was adjusted to 16 mg C_{XG}/cm². For ink preparation 384 mg (calculated with respect to 16 cm² area of Toray paper) C_{XG} was taken in a vial. 30ml of 3:7 isopropanol/water mixture was added into the vial followed by adding 71.06 mg of 60 wt.% PTFE. The solution was dispersed by ULTRA-TURRAX at 17000 rpm for 5 min (figure 7). ULTRA-TURRAX is a machine used for homogenizing and dispersing of pre-mixed liquid-liquid or solid-liquid substances¹⁴.

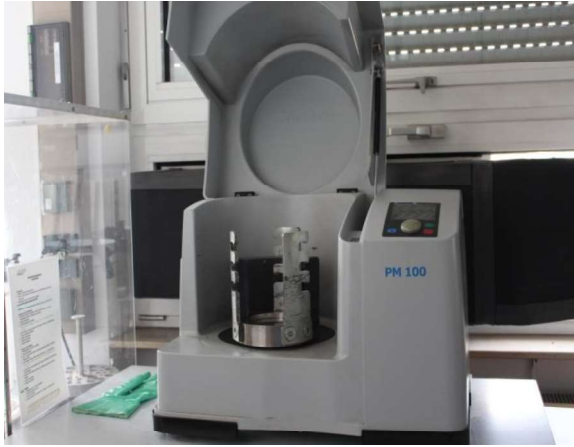


Figure 6: Ball Miller



Figure 7: Ultra Turrax machine

2.2.2. Spray coating

In the presented study, spray coating technique was used to achieve cathode electrode for test in Al ion battery.

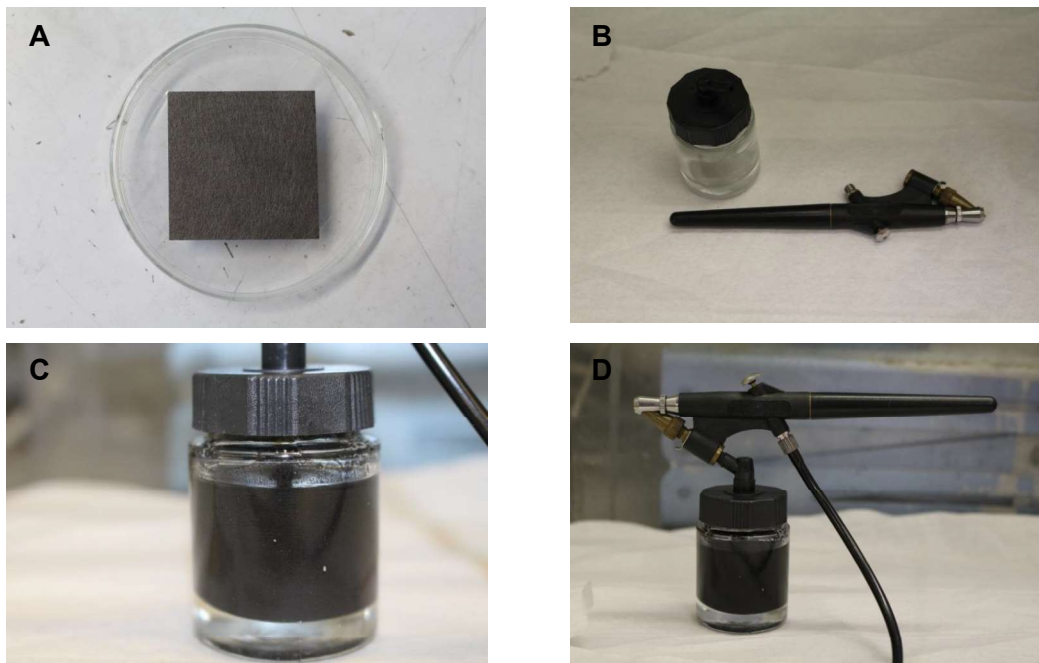


Figure 8: Spray coating of C_{xG} ink on Toray carbon paper A) Substrate arrangement B) air brush kit C) C_{xG} ink D) Air brush attached to compressor air regulator and ink jar

In this method, an airbrush pen was used for spraying to get layer by layer coating of selected C_{xG} on Toray paper (TGP-H-060) substrate. Toray paper was fixed on a

petri dish (figure 8A). In the setup, air brush spray gun was fixed to a glass jar containing ink and was connected to compressor air regulator (figure 8D). Compressor air pressure was set to about 0.4 bar-0.5 bar and with the help of air brush, ink was sprayed carefully on Toray paper. In order to achieve smooth coating, the distance between substrate and air brush was always maintained constant during spraying. In this way, thin films of C_{XGS} R/C₅₀, R/C₅₀₀, R/C₁₀₀₀, R/C₁₅₀₀, R/C₂₀₀₀, and R/C₂₅₀₀ were obtained on Toray paper. All coated C_{XGS} were then dried in the oven at 80°C for 24 h. Active material was noted for each electrode after drying. Table 3 shows the active material mass of R/C₅₀, R/C₅₀₀, R/C₁₀₀₀, R/C₁₅₀₀, R/C₂₀₀₀, and R/C₂₅₀₀ C_{XGS} . After drying, cathodes were cut in 18 mm diameter (area of electrode after cutting = 2.54cm²) with the help of punching instrument (figure 9). Later the cathodes were dried in vacuum atmosphere (p= 0.2 mbar) for 24h and at 125°C and then transferred to an Ar-filled glove box (MBRAUN UNIlab plus ECO), by taking care not to expose cathodes to air. For electrochemical measurements, EL cells were prepared in glove box (figure 10A).

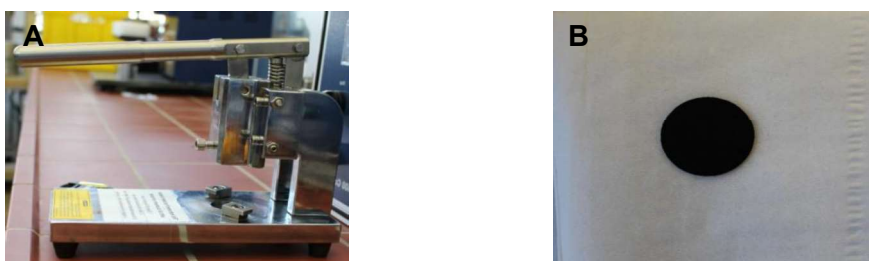


Figure 9: A) compact precision disc cutter B) 18mm coated toray carbon paper with C_{XG}

Table 3: Active material (C_{XG}) mass with respect to their corresponding R/C value

R/C	50	500	1000	1500	2000	2500
Active material mass mg/cm ²	8.24	13.65	11.07	12.45	15.195	12.34

2.2.3. Electrochemical measurement setup

Equipments / Chemicals	Manufacturer
Electrochemical Test-Cell	EL-cell
Al wire (reference)	<u>ChemPUR</u>
Al foil (anode)	ChemPUR
Glass fiber (separator)	EL-cell
AlCl_3 /[EMIm]Cl (1:1.5) (electrolyte)	<u>Lolitech</u>

Electrochemical measurements were carried out with the help of Bio-Logic BCS-810 potentiostat. Since AlCl_3 is highly reactive with oxygen and water, cells were assembled in a dry Ar-filled glovebox (UNIlab plus ECO, MBraun) with $p(\text{O}_2:\text{Ar}) \leq 0.1$ ppm and EL cells were used to make sure that AlCl_3 could not react with oxygen and water outside the glove box. EL cells are used for electrochemical characterization of battery system in which aprotic electrolyte is involved. An EL cell design accommodates a counter electrode (Al foil) on the cell bottom, a working electrode on top and separator in between. A piece of reference material (Al wire) is also loaded in REF sleeve through hole. The reference material is contacted from outside by means of the spring loaded contact pin¹⁵. A schematic diagram of an EL cell is shown below (figure 10B)-

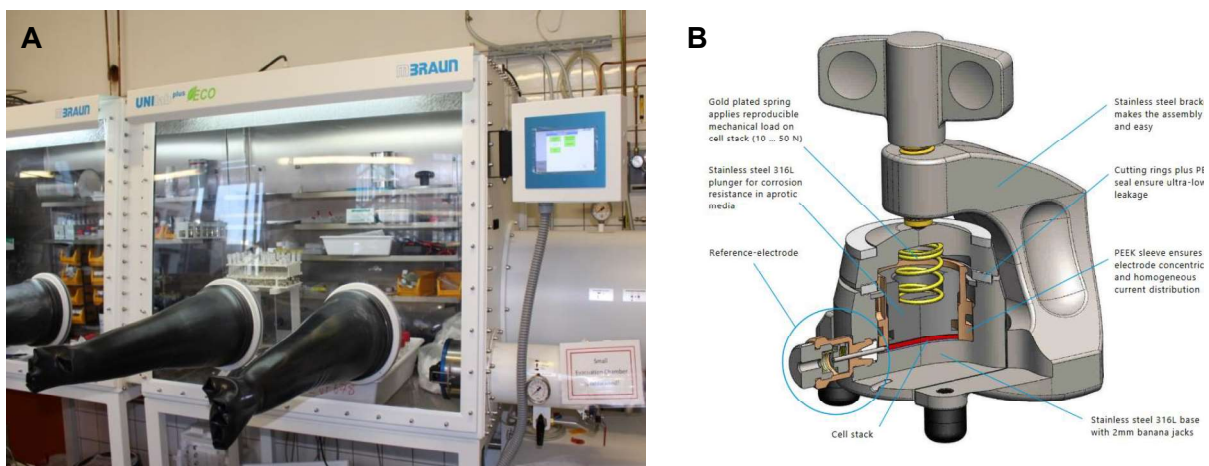


Figure 10: A) Glove box B) Schematic diagram of ELcell¹⁵

For all electrochemical measurements, Al wire (ChemPUR) was used as reference electrode, an Al foil with thickness of 0.25 mm and diameter of 18 mm from ChemPUR was used as anode, glass fiber (EL-Cell) as separator and Toray paper (TGP-H-060) was used as current collector. The electrolyte solution was light yellow 1:1.5 anhydrous AlCl_3 in 1-ethyl-3-methylimidazolium chloride ($\text{AlCl}_3 / [\text{EMIm}]\text{Cl} = 1:1.5$). The amount of electrolyte used was 250 μl . C_{XGs} with R/C values 50, 500, 1000, 1500, 2000, and 2500 were tested as working electrodes having surface area of 2.54 cm^2 and active mass of these electrodes are given in table 3. All electrochemical measurements were carried out at room temperature and all capacities were reported per mass of the active material.

2.2.4. Galvanostatic charge / discharge measurements of AIB

Galvanostatic charge-discharge tests were performed at different current densities with the cutoff potential window 0.5 V to 2.5 V by using BioLogic (BCS-810) instrument. The experiment was performed by applying increasing currents- 0.5 mA, 1 mA, 1.5 mA, 2 mA, 2.5 mA, 3 mA, 3.5 mA, 4 mA, 4.5 mA, and 5 mA (forward scan) and then reverse currents were applied from 5 mA to 0.5 mA (backward scan). For each current rate the cutoff voltage was kept same (0.5 V to 2.5 V) and charging time was optimized. 2 h 48 min, 1h, 48 min, 1 h, 48 min, 40 min, 34 min, 30 min, 27 min and 24 min of charging was setup for 0.5 mA, 1 mA, 1.5 mA, 2 mA, 2.5 mA, 3 mA, 3.5 mA, 4 mA, 4.5 mA, and 5 mA current respectively. Figure 11 shows the galvanostatic charge-discharge measurement setup in which red wire was connected to cathode and blue wire was connected to anode.

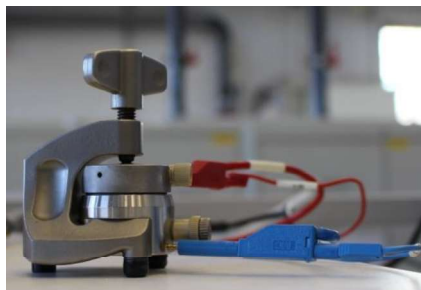


Figure 11: Galvanostatic charge-discharge measurement setup

2.2.5. Cyclic voltammetry (CV)

CV measurements were carried out in the voltage window between 0.7 V to 2.5 V vs Al/Al³⁺ at 10 mV/s scan rate.

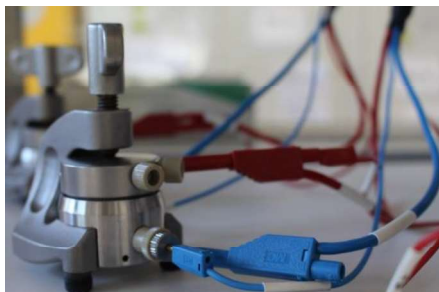


Figure 12: Half-cell CV measurement setup

Right after experiment EL-cell were disassembled in the reverse order of assembly. Anode, cathode and separator were washed with isopropanol followed by washing with ultra-pure water. Spare parts of the cells were washed with ethanol solution with ultra-sonic bath for 20 min and then washed two more times by Millipore water in sonication bath.

2.3. Experimental Section 3: Characterization techniques for C_{XGs}

Several methods were employed to characterize C_{XGs} properties and surface area information:

2.3.1. Thermogravimetric analysis (TGA)

Thermo gravimetric Analysis is a technique in which the mass of a substance is monitored as a function of temperature or time as the sample specimen is subjected to a controlled temperature program in a controlled atmosphere. An Alternate Definition: TGA is a technique in which, upon heating a material, its weight increases or decreases. A Simple TGA Concept is it measures a sample's weight as it is heated or cooled in a furnace.

A TGA consists of a sample pan that is supported by a precision balance. That pan resides in a furnace and is heated or cooled during the experiment. The mass of the sample is monitored during the experiment. A sample purge gas controls the sample

environment. This gas may be inert or a reactive gas that flows over the sample and exits through an exhaust.

This method allows to quantify mass loss of sample due to water/solvent evaporation, decarboxylation, pyrolysis, oxidation/reduction reactions, decomposition of plasticizer, pore former. All these quantifiable applications are usually done upon heating, but there are some experiments where information may be obtained upon cooling¹⁶.



Figure 13: Simultaneous Thermogravimetry-Differential Scanning Calorimetry

In the scope of this thesis, TGA analysis of all C_{XG_s} was carried out using NETZSCH STA H49 F3 Jupiter instrument (figure 13) under both N_2 and Ar atmosphere to understand the undergoing chemical processes during pyrolysis. About 30 mg to 40 mg C_{XG} samples was taken in TGA alumina crucible. The temperature was risen till $400^\circ C$ then the temperature was hold constant for 2 h and then again was risen till $800^\circ C$. The heating rate was 5 K/min and cooling rate was 10 K/min.

2.3.2. Scanning electron microscopy (SEM)

The overall design of an electron microscope is similar to that of a light microscope. In the electron microscope, the light is substituted with electrons and the glass lenses are substituted with electromagnetic/electrostatic lenses. Figure 14 (A) shows a column structure of a conventional SEM.

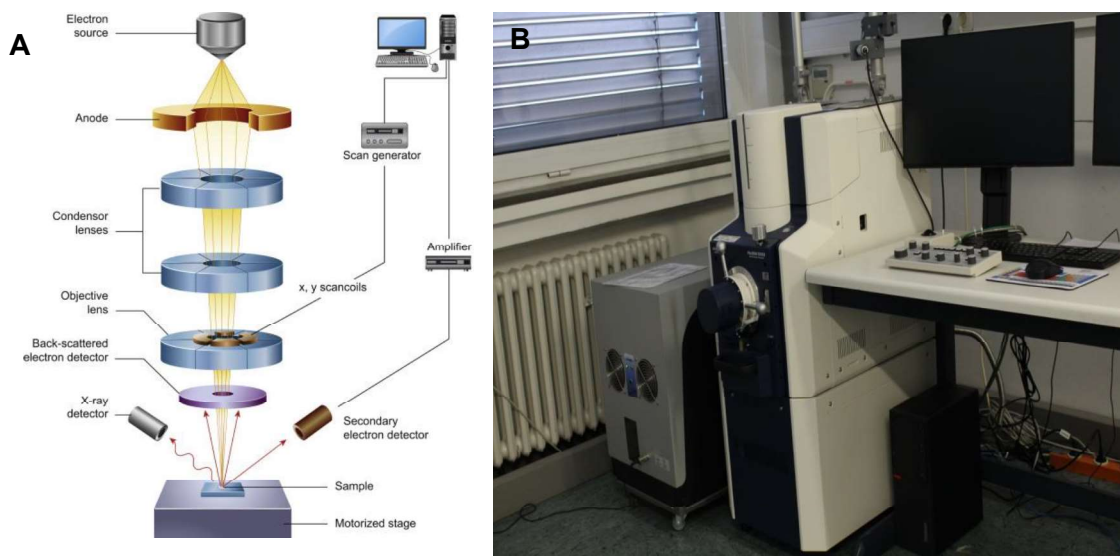


Figure 14: A) Column structure of SEM¹⁷ B) SEM analyzer

An electron beam is formed at the tip of a heated filament. The electrons are accelerated with voltages between 0.2 – 30 kV and are guided through the scanning electron microscope column by electromagnetic lenses. The beam is focused in the objective lens and a small beam spot is moved/scanned over the specimen surface using deflector coils. The beam interacts with the specimen and emitted electrons are detected in specific detectors and amplified using photomultiplier tubes. Emitted radiation as x-rays is detected in according detectors. Every scanned pixel on the specimen represents a pixel on the screen

Electron microscopes are high-vacuum systems. In the area of the electron source a vacuum of 10^{-5} mbar to 10^{-10} mbar has to be maintained. The mean free path, referred to as the distance a molecule can fly before hitting another particle, accounts to about 50 meters at a vacuum of 10^{-6} mbar. Any collision with a residual gas molecule in the system reduces the resolution and performance by scattering of electrons.

The vacuum system of an electron microscope consists of a cascade of low and high vacuum pumps¹⁸.

- Image Formation

In SEM, mainly secondary electrons are used for imaging of biological specimens. These electrons have a very low energy (around 50 eV) compared to the energy of the primary electrons (up to 30 keV). Due to the low energy, these electrons can escape only from the surface area of the specimen and therefore provide information about the surface topography. They are detected with an Everhart Thornley detector. The SE is collected by a collector grid. A voltage of + 200 to 500 V is applied to the collector grid which attracts the low energy electrons. The SE then hit a scintillator which converts the electrons to photons. The photons are guided by a light conducting tube on the photomultiplier tube, where the photons again are converted to electrons that are amplified finally leading to an electrical signal. The current is translated into a gray value and displayed on the screen of the monitor²¹.

2.3.3. X-ray diffraction (XRD)

X-ray diffraction is the most common technique for determining the structure of crystal and atomic spacing. It is based on constructive interference of monochromatic X-rays that are in phase. Figure 15 shows how diffraction of x-rays by crystal planes allows one to derive lattice spacing by using the Bragg's law.

$$n\lambda = 2d \sin\theta$$

where-

n= order of reflection

λ = wavelength of x-rays

d= spacing between the crystal planes of a given sample

θ = diffraction angle

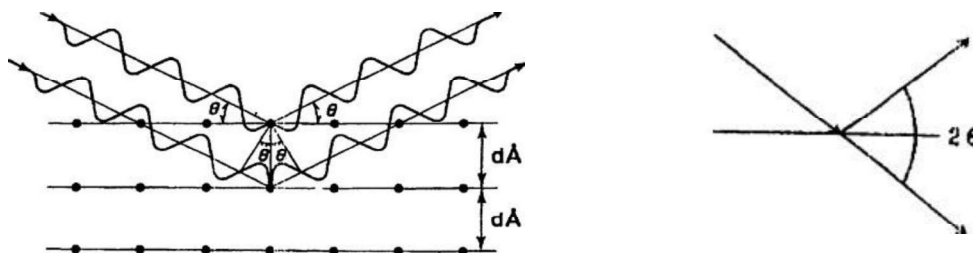


Figure 15: Schematic representation of Bragg's Law²²

Bragg's law relates the wavelength of electromagnetic radiation to the diffraction angle and the lattice spacing in a crystalline sample. These diffracted X-rays are then detected, processed, and counted. By scanning the sample through a range of 2θ angles, all possible diffraction directions of the lattice should be attained due to the random orientation of the powdered material. Conversion of the diffraction peaks to d-spacings allows identification of the compound because each compound has a set of unique d-spacings. Typically, this is achieved by comparison of d-spacings with standard reference patterns.

X-ray diffractometers consist of three basic elements that are x-rays tube, sample holder and detector. X-rays are generated in a cathode ray tube by heating a filament to produce electrons. Certain voltage is applied so that electrons can accelerate and bombard with the sample. Characteristic x-ray spectra are produced when bombarded electrons with sufficient energy displace the inner shell electrons. Based on the diffraction method one may address the number of compounds encountered in nature exhibiting a crystalline structure that is composed of atoms arranged in a regular strictly structured manner determined by the crystallographic phase²³.

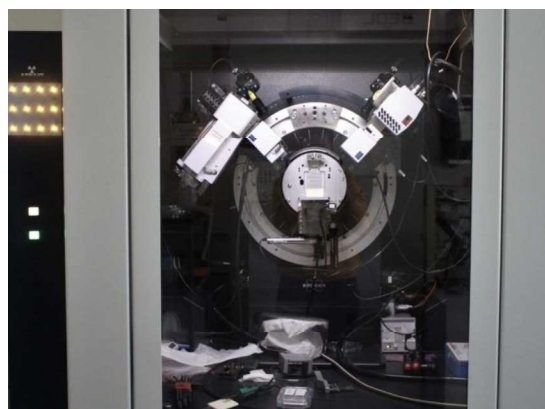


Figure 16: XRD analyser for powder C_{XG} sample

For C_{XG} system, X-ray diffraction pattern were collected with a diffract meter (Bruker D8) (figure 16). About 20 mg of C_{XG} powder was loaded on a clean glass slide and the surface was flattened. The sample was mounted on the XRD sample stage and properly aligned with the help of red laser beam. The XRD was performed using Cu-K-alpha source with $\lambda = 0.154\text{nm}$. The X-ray power employed was 1.6 kW. The XRD was scanned in 2θ ranges from 10° to 90° with an increment of 0.02° and 1.5 s for each step.

2.3.4. Raman spectroscopy

Raman spectroscopy is based on the inelastic light scattering in a substance where the incident light transfers energy to molecular vibrations. In Raman spectroscopy infrared light (IR) and visible light are used for the excitation. When an intense light source for example a laser hits a sample, part of the light will be scattered in different directions. This scattering of light can be elastic or inelastic. In elastic scattering, the scattered light has the same frequency as the incident light. However, during inelastic interaction incident light beam exchange some energy with material. Raman spectroscopy is based on Raman Effect which states- the frequency of a small fraction of scattered radiation is different from frequency of monochromatic incident radiation.

There are three scattering processes that are important for Raman Spectroscopy-

- 1) Rayleigh Scattering - When a monochromatic light source hits at the sample, it scattered in all the direction. Much of this scattered radiation has a same frequency as incident radiation (elastic scattering), forms Rayleigh scattering.
- 2) Stokes Raman Scattering- It is the inelastic scattering process that transfers energy from the light to vibration of the molecules. Therefore, the frequency of the incident radiation is higher than the scattered radiation.
- 3) Anti-Stokes Raman Scattering - It is another inelastic scattering where a small portion of energy from vibrating molecules transfers to the incident photon. Therefore the frequency of incident radiation is lower than scattered radiation²⁴.

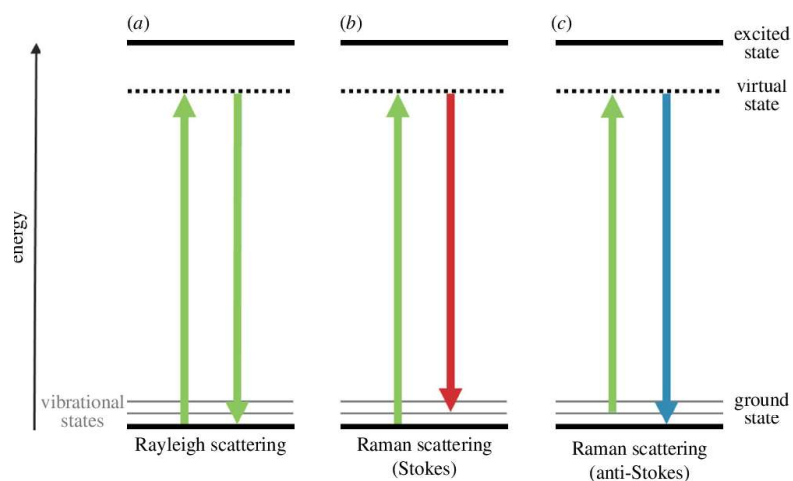


Figure 17: Schematic diagram of the energy transitions involved in a) Rayleigh scattering, b-c) Raman stokes and anti-stokes scatterings²⁵

Raman spectroscopy is different from IR spectroscopy as IR measures the dipole but polarizability change can only be determined by Raman spectroscopy.



Figure 18: Confocal RAMAN microscope

For all the samples, the Raman spectra were recorded on a **Renishaw inVia confocal microscope** equipped with a 532 nm laser source. Experimental spectrum was recorded with 5% laser power, 10 s of exposure time and with 20 accumulations.

2.3.5. Brunauer-Emmett-Teller (BET)

Physisorption or physical adsorption, is the process by which gas and vapor atoms and molecules are adsorbed onto the surface of solid by weak attractive forces like Van der Waals force. Gas adsorption on porous and finely dispersed solid is an appropriate method to measure the specific surface area, pore size and pore volume distribution.

Freundlich adsorption isotherm, Langmuir adsorption isotherm, Temkin adsorption isotherms and BET adsorption isotherm are four common models of adsorption isotherms in which BET adsorption isotherm is most common and most widely used. It explains the multilayer adsorption of gas molecules under high pressure and low temperature conditions. The BET equation is given as¹⁰-

$$V_{total} = \frac{V_{mono} C \left(\frac{P}{P_0} \right)}{\left(1 - \frac{P}{P_0} \right) \left(1 + C \left(\frac{P}{P_0} \right) - \frac{P}{P_0} \right)}$$

- **Micro and Mesoporous Isotherms**

The first important information about surface and porosity obtained from a physisorption experiment is the isotherm. It can reveal the kind of porosity present in unknown samples. Brunauer has defined five different types as shown below:

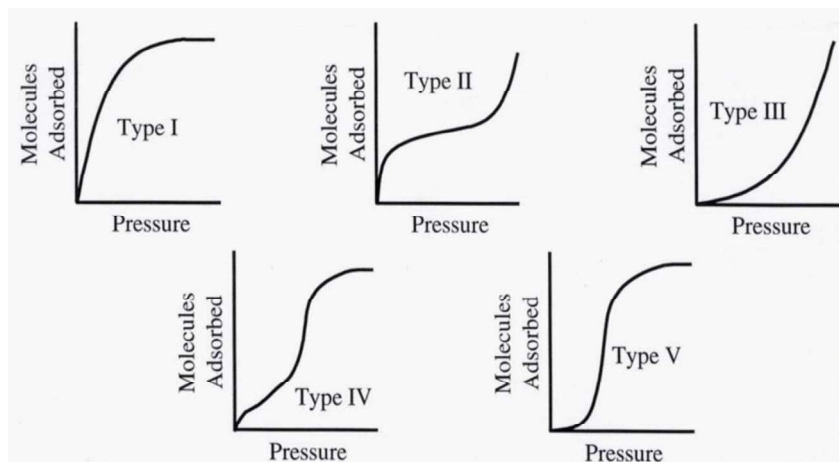


Figure 19: Adsorption isotherm types defined by Brunauer¹¹

2.4. Electrochemical Characterization Techniques

2.4.1. Cyclic Voltammetry (CV)

The current, resulting from applied potential is measured during a potential sweep that results in a current-potential plot known as cyclic voltammogram. If we assume that initially there is only species 'O' present in reaction media, a negative potential sweep causes reduction of 'O' to 'R'. As potential approaches to E° for the redox process, a cathodic current is observed until a peak is reached. It is the time when all O converts to R and gives maximum current but as one keeps apply negative potential and there is no more O to convert in R, diffusion layer starts growing the current starts dropping (figure 20 (B-C)). While during the reverse scan (positive) species 'R' re-oxidizes to 'O' near the electrode surface, results in an anodic peak current (figure 18). Anodic peak current (i_{pa}), cathodic peak current (i_{pc}), anodic peak potential (E_{pa}) and cathodic peak potential (E_{pc}) are characteristic parameters of cyclic voltammogram²⁶.

For a reversible system peak current is given by the Randles-Sevcik equation at 25°C.

$$i_p = (2.69 \cdot 10^5) n^{3/2} A C D^{1/2} v^{1/2}$$

n is the number of electrons, A is electrode area (cm^2), C is concentration (mol/cm^3), D is diffusion coefficient (cm^2/s) and v is potential scan rate (V/s).

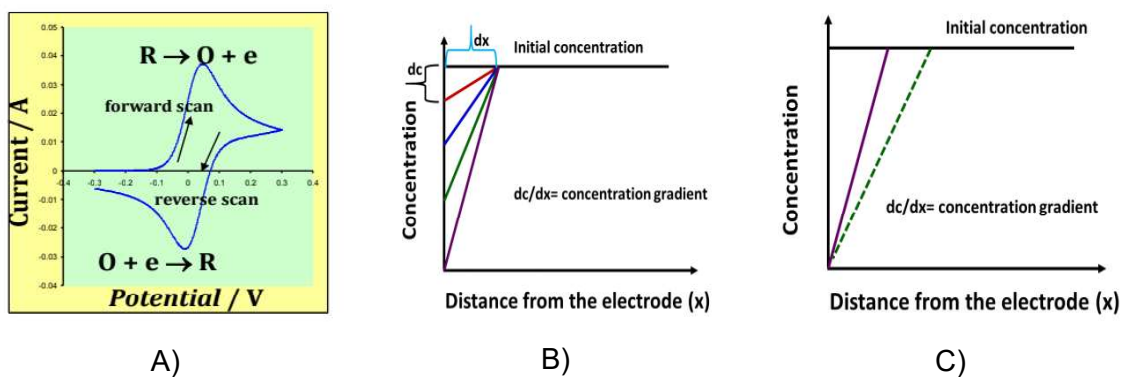


Figure 20: A) Cyclic voltammogram B) and C) concentration profile. variation of the concentration of electroactive species with the distance x measured from electrode surface at different potential

2.4.2. Galvanostatic Charge Discharge (GCD)

Galvanostatic charge-discharge is an electrochemical method to evaluate the electrochemical capacitance and cycle life of batteries and supercapacitors under controlled current conditions. In this technique a current pulse is applied to the working and the resulting potential is measured against a reference electrode as a function of time. A continuous repetition of charge-discharge on positive (anode) and negative (cathode) electrodes are performed for equal times and by applying positive and negative current of the same magnitude until a set voltage is reached. Therefore, in an ideal case one obtains a symmetric triangular voltage wave. But in a real case when current is applied the measured potential is abruptly changes due to the IR loss voltage anodic branch of the voltage wave voltage drop after completion of charging step can be seen ²⁷.

3. RESULTS AND DISCUSSIONS

3.1. Carbon Xerogel Synthesis

Figure 21 shows the xerogel suspension, powder form before pyrolysis and xerogels after pyrolysis (C_{XG}). It is observed that all synthesized xerogels have different colors before carbonization. Exceptionally sample R/C₅₀ was obtained as translucent dark red in color having a solid monolith structure and other xerogels with higher R/C ratio were opaque and brown with different shades. The reason of different color may relate to the different pH of the systems (see Fig. 4 in section 2.1.2). As reported from the literature, it is proved that higher pH (low R/C value) of initial solution leads to the quick formation resorcinol anions (highly catalytic system) and therefore extremely branched and crosslinked cluster forms which leads to the smaller and more interconnected polymer particles. As R/C ratio increases, the reaction between resorcinol and formaldehyde slows down hence less branched cluster forms which persists longer in the nucleation regime leads the formation of large clusters^{25,26}. The final product (carbon xerogel) was obtained after vacuum drying followed by pyrolysis at 800°C.



Figure 21: From top to bottom: Xerogels in suspension (R/C₅₀-R/C₂₀₀₀₀) and powder form and Xerogels after carbonization (C_{XGs})

Particle size, morphology, crystallinity, temperature stability, pore size and surface area of these powder samples were examined by using XRD, Raman, SEM, TGA, DSC and BET techniques. Later, electrochemical characterization (galvanostatic charge-discharge, and cyclic voltammetry) were carried out in EL cells.

3.2. Thermal Degradation of Xerogel during Carbonization in TGA apparatus

TGA was performed to observe the mass loss behavior of xerogel with increasing temperature during carbonization. Figure 22 shows the mass loss and DTA profile of R/C₅₀ xerogel with increasing temperature. The temperature profile was identical to that during pyrolysis of xerogel samples in tubular oven.

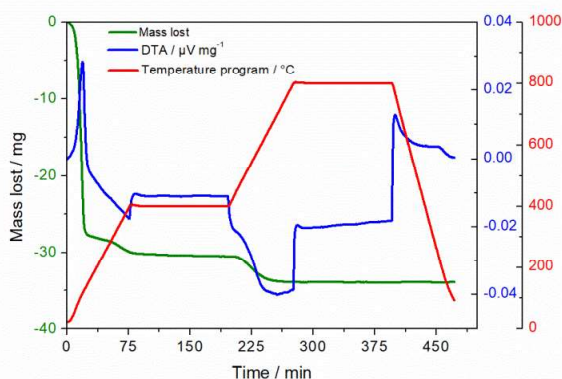


Figure 22: TGA curve for R/C₅₀ xerogel in Argon atmosphere

Resorcinol-formaldehyde decomposition was found to occur in four stages, with the initial stage involving water evaporation till 135 °C with an endothermic peak in DTA curve. The second stage involving evaporation of other solvents like methanol and unreacted formaldehyde (~ 135 °C - 250 °C) with an exothermic DTA peak. Third stage of mass loss was occurred in the temperature range 250 °C - 400 °C which is caused by the decomposition of ether crosslinks with an exothermic DTA peak. During the 1st isotherm step (400 °C), no mass change was observed indicated by flat DTA curve. During the 2nd heat ramp until 800 °C, the gel finally starts to carbonize, indicated by a strong exothermic process in DTA curve. Mass loss in this range was caused by decomposition of methylene bridges and rupture of resorcinol-hydroxyl functional groups. During the 2nd isotherm (800 °C) the DTA curve is flat and no mass loss was observed²⁶.

3.3. Surface Characterization of C_{XGs}

Raman spectra elucidated on the carbonized xerogels (C_{XGs}). All samples pyrolyzed at 800°C show typical spectrum of carbonized materials which is characterized by the ideal graphitic lattice G-band (1580 cm^{-1}) and the defect related D-band (1350 cm^{-1})²⁷.

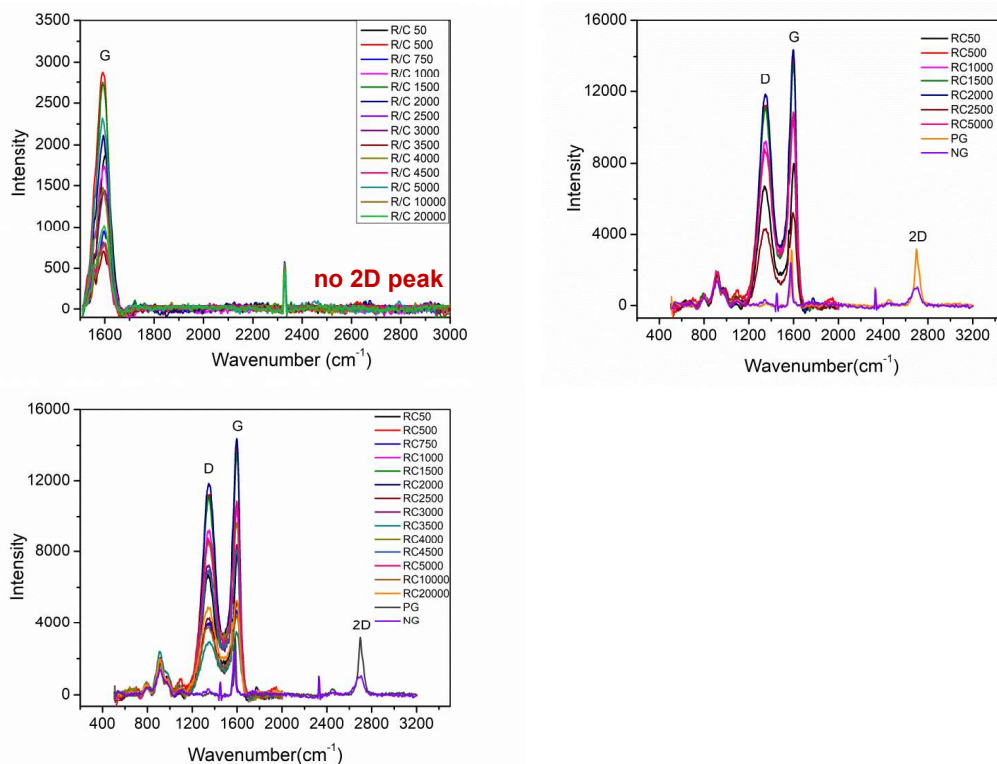


Figure 23: Raman spectra of all prepared C_{XGs} as well as pyrolytic graphite (PG) and natural graphite (NG) as references

Xerogels contain a number of functional groups which are lost during pyrolysis, thus giving rise to the graphitic (G-band) and defect domain (D-band) of carbon in figure 23. The D band is obtained at 1352 cm^{-1} and G band is obtained at wavenumber 1598 cm^{-1} . The intensity ratio of D band to G band (I_D/I_G) provides qualitative information about the graphitic content in carbon materials. The I_D/I_G values for all C_{XGs} are presented in table 4. These values are between 0.8-0.9 that shows that the pyrolyzed samples have predominant graphitic domains which is advantageous for cathode material in Al ion battery. D and G bands show different intensities for different R/C value. R/C₂₀₀₀ shows highest intensity followed by R/C₅₀₀, R/C₁₅₀₀, R/C₅₀₀₀ and R/C₁₀₀₀. The reason for low peak intensity in Raman spectra might be

due to less crosslinking structure at high R/C value and hence lesser number of sp^3 and sp^2 -hybridized carbons. Because of this reason, C_{XG} samples with R/C values higher than 2500 were not further considered for electrochemical investigations. R/C_{750} is also showing very less intensity of D and G bands, consequently only R/C_{50} , R/C_{500} , R/C_{1000} , R/C_{1500} , R/C_{2000} , and R/C_{2500} were selected for further studies. The Raman spectra of all C_{XGs} is presented in figure 23.

Table 4: I_D/I_G ratio with their respective R/C value

R/C	50	500	750	1000	1500	2000	2500	3000	3500	4000	4500	5000	10000	20000
I_D/I_G	0.85	0.80	0.84	0.88	0.82	0.82	0.86	0.86	0.83	0.88	0.86	0.80	0.83	0.91

2D peak in Raman spectra is the characteristic of graphite or graphene structure. In Raman spectra of natural graphite (NG) and pyrolytic graphite (PG), we clearly see the 2D peak which represents the second order stacking of graphene layers.

In C_{XG} 's Raman spectra, there is no 2D peak indicates C_{XGs} do not have graphene in its growth. The presence of D and G band indicates the presence of sp^2 carbon with a lot of defects which basically refers to the sp^3 amorphous carbon.

A comparison of the XRD spectra of as-prepared C_{XGs} and Natural Graphite (NG) in figure 24 is presented. Since NG has periodicity of atoms in its structure hence in the XRD pattern of NG (figure 24), narrow characteristic peaks of (002) at 26.50° , (101) at 42.31° and (004) at 54.60° were observed.

In order to check the crystallinity of C_{XGs} , XRD data of C_{XGs} was compared with NG. In the case of C_{XGs} , wide bumps distributed in a wide range of 2θ were observed instead of high intensity sharp peaks. It represents that x-rays have scattered in various direction in C_{XG} because of not having periodic arrangement of atoms. In C_{XG} 's XRD pattern there are three broad peaks present in the 2θ range of 10° - 30° and 40° - 50° but no sharp peak as NG, depicts absence of periodic arrangement of atoms and hence the material is totally amorphous.

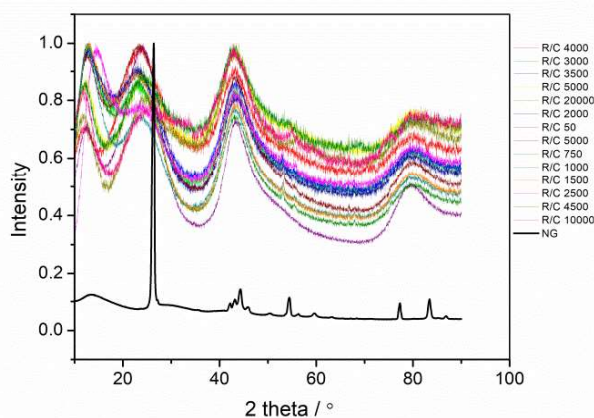


Figure 24: XRD diffraction pattern of as-prepared carbon xerogels (C_{xG}) with natural graphite as reference

3.4. Effect of Resorcinol/Catalyst Ratio (R/C) on Porous Structure

To check how R/C ratio and consequently pH value influence the pore texture of pyrolyzed xerogels, R/C_{500} and R/C_{2500} were characterized by means of nitrogen physisorption technique at -196°C (Quantichrome Autosorb iQ₃). Figure 25 shows nitrogen adsorption-desorption isotherm of R/C_{500} and R/C_{2500} .

C_{xG} obtained from R/C_{500} was micro-mesoporous (combination of type I and type IV isotherm) while R/C_{2500} shows type I isotherm which belongs to microporous structure. Hysteresis loop in R/C_{500} clearly indicates monolayer - multilayer adsorption with capillary condensation (phenomenon whereby a gas condenses to a liquid phase in a pore at pressure less than the saturation pressure P_0 of the bulk fluid) and hence presence of mesopores. The lower part of hysteresis shows adsorption while upper part indicates desorption of gas molecules. However, adsorption branch of R/C_{500} isotherm resembles with type I isotherm it means R/C_{500} possess both micro and meso pores. In R/C_{500} isotherm curve, we see that at low relative pressure, a monolayer is formed while as isotherm proceed to higher relative pressure, we observe a sloped region in the curve, indicates the formation of multilayers. However, after certain relative pressure, the film thickness cannot be exceeded more, hence desorption starts. In addition, R/C_{2500} shows lower adsorption capacity than R/C_{500} at low pressure shows that R/C_{2500} has less micro porosity than R/C_{500} .

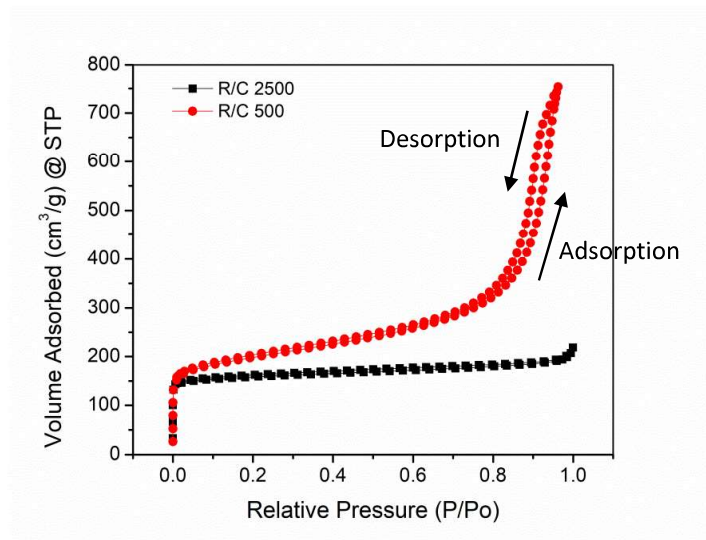


Figure 25: Isotherm curves of R/C_{500} and R/C_{2500}

The results confirm that pore size distribution of C_{XGS} can be obtained by tuning the amount of catalyst. However, in this thesis, BET data of only two C_{XGS} (R/C_{500} and R/C_{2500}) is presented because of restricted accessibility to BET apparatus. Therefore, a founded comment regarding the relation between pore texture and R/C values can only be made after comparing all R/C values isotherms.

3.5. Pore Size Distribution

In figure 26, the pore size distribution of R/C_{500} and R/C_{2500} is shown. As discussed above for R/C_{500} , pore size is distributed in micro (< 2 nm) and mesopores (between 2-50 nm), regions, it is clear with pore size distribution curve. R/C_{500} shows a sharp peak in microporous region and a bump in mesoporous region (< 2 nm) in figure 26. Most of the pores are mesopores because their pore size is between 2-30 nm pore width regions. In R/C_{2500} , there is a sharp peak at 0.8 nm pore width and a very tiny peak at 2 nm pore width indicates the high amount of micropores present in R/C_{2500} . However, we see some mesopores, but the number of mesopores is lesser than micropores. Figure 26(C) shows the comparative pore size distribution curves of R/C_{500} and R/C_{2500} .

By the BET data of R/C_{500} and R/C_{2500} we can say that increasing pH or decreasing R/C ratio is affecting the pore size and surface area of material. According to the addition-condensation scheme governing the system, the average pore size decreases when the R/C ratio decreases²⁵. Here we observe the same in table 5.

The surface area of C_{XG} has increased from $625 \text{ m}^2\text{g}^{-1}$ for R/C_{2500} to $720 \text{ m}^2\text{g}^{-1}$ for R/C_{500} .

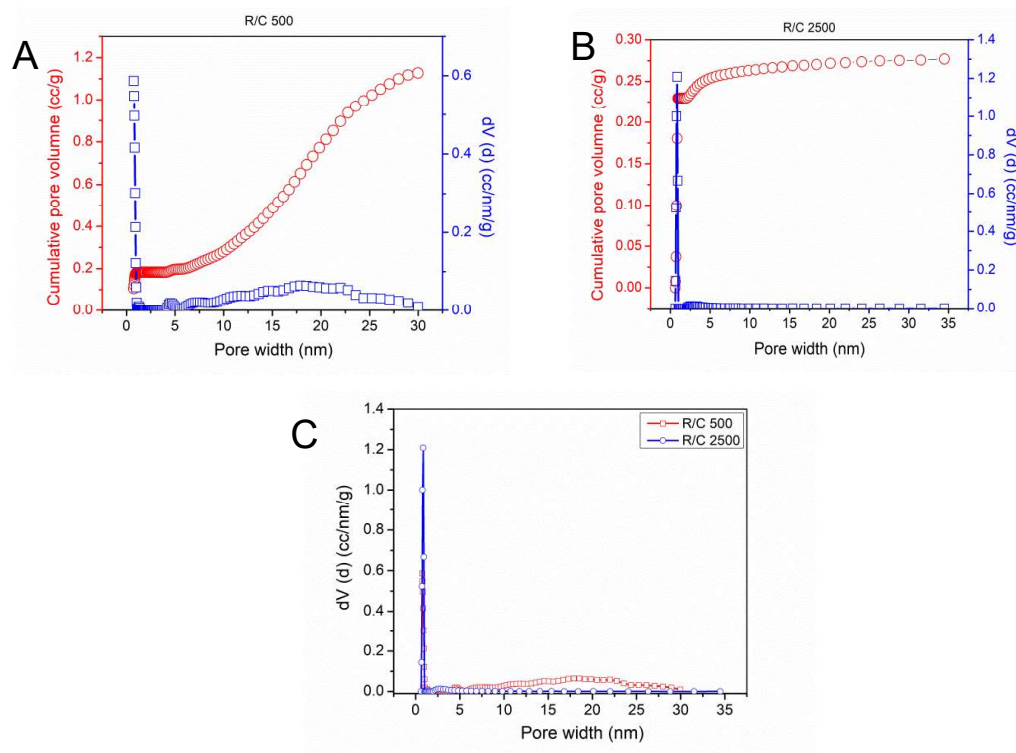


Figure 26: Pore size distribution of A) R/C_{500} B) R/C_{2500} . C) comparison R/C_{500} and R/C_{2500}

Table 5: pore texture properties of R/C_{500} and R/C_{2500}

R/C	S_{BET} m^2/g	Pore Volume cc/g	V_{micro} cc/g	Avg Pore width nm
500	720	1.13	0.173	8.41
2500	625	0.277	0.216	8.45

3.6. Scanning Electron Microscopy (SEM) of C_{XGs}

The morphology of pyrolyzed R/C_{50} , R/C_{500} , R/C_{1000} , R/C_{1500} , R/C_{2000} and R/C_{2500} samples after ball milling was observed by scanning electron microscopy (SEM) in figure 27. It appears that C_{XGs} particles are not spherical but irregular in shape with sharp edges. We see a big block with a lot of small particles in R/C_{50} . This is due to

breaking of monolith in R/C₅₀ and R/C₅₀₀ during ball milling. The parallel lines in R/C₅₀ C_{XG} are fractures generated by monolith breaking. Additionally, the particles are bigger in R/C₅₀ and R/C₁₀₀₀ than other C_{XG}s. Ball milling procedure has to be improved to get more homogeneous powder material. The surface of R/C₁₀₀₀, R/C₁₅₀₀, R/C₂₀₀₀ and R/C₂₅₀₀ looks smooth at low magnification level. As mentioned in the literature²⁸, carbon C_{XG}s are made of three-dimensional interconnected particles with micro, meso and macropores depending of synthesis parameter such as pH and pyrolysis temperature. Hardness of carbon structure is determined by pore size distribution.

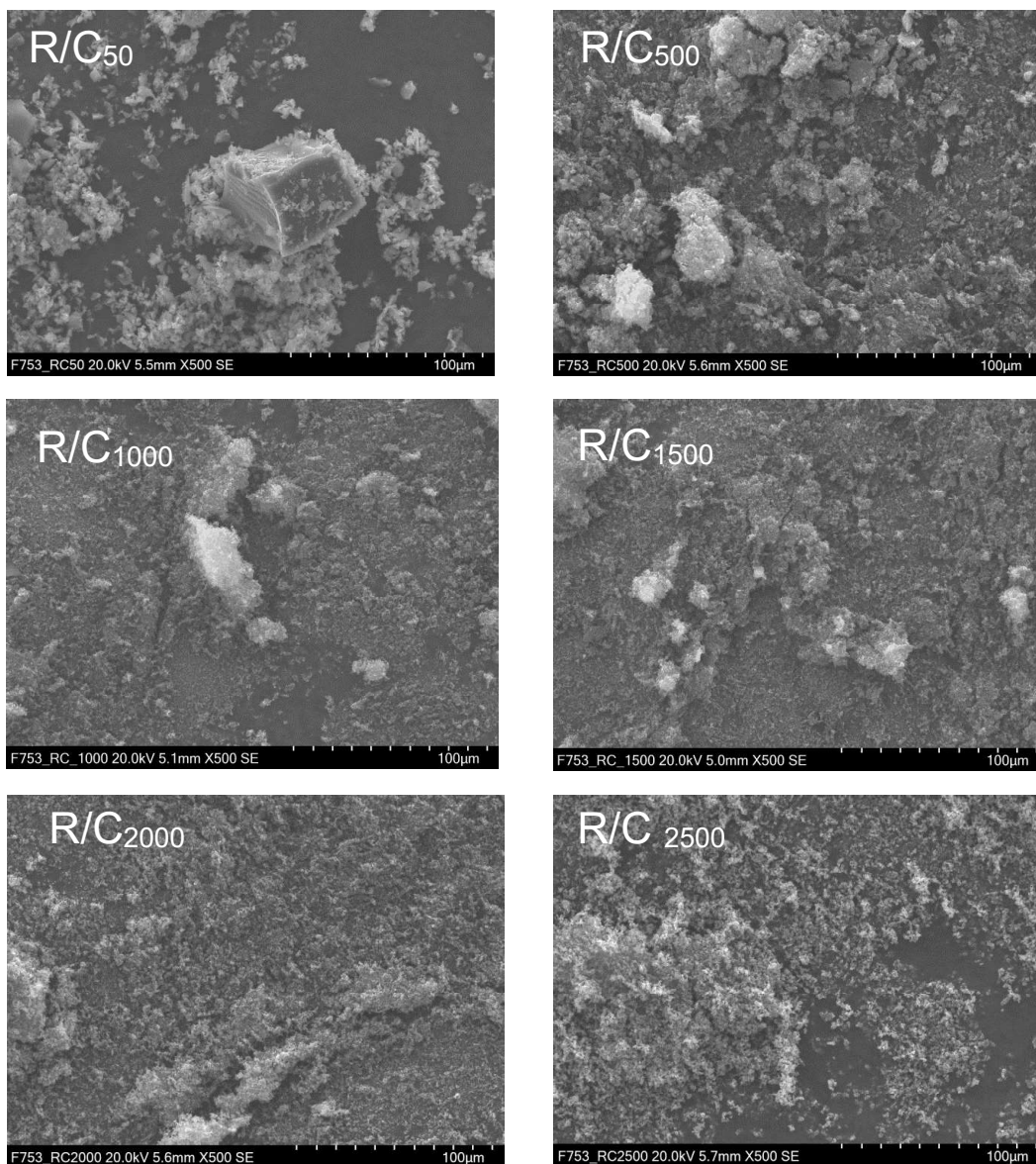


Figure 27: SEM images of selected carbon xerogels

3.7. Electrochemical Performance of AIB Cell with Carbon Xerogel

The feasibility of some selected C_{XGS} (R/C₅₀, 500, 1000, 1500, 2000, and 2500) as intercalation material for aluminum ions was investigated by cyclic voltammetry and galvanostatic charge-discharge experiments in 1:1.5 EMImCl/AlCl₃ at room temperature.

3.7.1. Half-cell measurements

Figure 28(A) depicts the cyclic voltammetry (CV) curve of R/C₅₀, 500, 1000, 1500, 2000, and 2500 carbon xerogels in 3-electrode EL-cell configuration with a scan rate of 10 mV/s between 0.7 V - 2.5 V. We observe a clear oxidation and reduction peak in all C_{XGS} showing the redox process induced by AlCl₄⁻ intercalation/deintercalation is reversible. In cells with R/C₅₀₀ and R/C₁₀₀₀, we see two oxidation peaks: One in the 2.5 - 2 V range and the other one around 1.3 V. These peaks are attributed to the intercalation of AlCl₄⁻ into C_{XGS} . During de-intercalation process C_{XGS} show peaks in 1.0 V to 1.5 V range, correspond to the extraction of AlCl₄⁻. In Figure 28(B), activity of Al deposition & dissolution on Al foil is shown. With increasing cycle number, current density of both reactions increased until reaching near steady-state. The induced charge of dissolution steps (anodic) is slightly inferior to that of deposition steps (cathodic), which is an indication for quasi-reversible process.

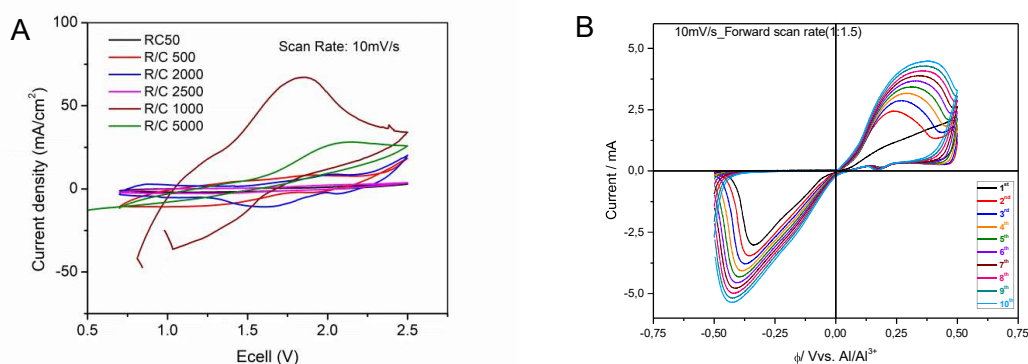


Figure 28: Cyclic Voltammetry (CV) curve of R/C₅₀, 500, 1000, 1500 and 2500 carbon xerogel (left) and CVs of Al dissolution / deposition in 1:1.5 EMImCl / AlCl₃ on Al foil at 10 mV/s (right) from Ms. B. Rana master thesis at DFI

3.7.2.2. Discharge capacity evaluation of AIB with R/C₅₀₀, R/C₁₀₀₀ and R/C₁₅₀₀

Notably, the carbon C_{XG} with R/C₅₀₀, R/C₁₀₀₀ and R/C₁₅₀₀ show excellent discharge capacities. AIB cell with R/C₅₀₀ shows 88 mAhg⁻¹ discharge capacity with 85% coulombic efficiency, R/C₁₀₀₀ shows 101 mAhg⁻¹ discharge capacity at 1.5 mA current with 82% coulombic efficiency whereas R/C₁₅₀₀ shows 96 mAhg⁻¹ discharge capacity with 84% coulombic efficiency at 0.5 mA current. Table 6 compares R/C₅₀₀, R/C₁₀₀₀, and R/C₁₅₀₀ discharge capacities and coulombic efficiency.

Table 6: Discharge capacity and coulombic efficiency (CE) comparison of R/C₅₀₀, R/C₁₀₀₀ and R/C₁₅₀₀

R/C ₅₀₀			R/C ₁₀₀₀			R/C ₁₅₀₀		
Current mA	Discharge Capacity mAhg ⁻¹	CE %	Current mA	Discharge Capacity mAhg ⁻¹	CE %	Current mA	Discharge Capacity mAhg ⁻¹	CE %
0.5	88	85	0.5	101	77	0.5	96	84
1	70	92	1	79	84	1	72	86
1.5	78	88	1.5	89	82	1.5	65	86
2	99	68	2	127	70	2	41	92
2.5	86	77	2.5	94	77	2.5	29	96
3	76	83	3	75	82	3	23	98
3.5	68	87	3.5	62	88	3.5	19	100
4	62	90	4	54	88	4	16	100
4.5	56	93	4.5	49	90	4.5	13	100
5	52	93	5	45	92	5	11	100

Discharge/charge capacities of AIB cells with R/C₅₀₀ are shown below in figure 30 with rate capability graph.

In the rate capability graphs (figure 30), most of the discharge capacity has almost regained as the current returns to 0.5 mA from 5 mA. At 1 mA current, the discharge capacity of R/C₅₀₀ was 70 mAhg⁻¹, that reduces to 62 mAhg⁻¹.

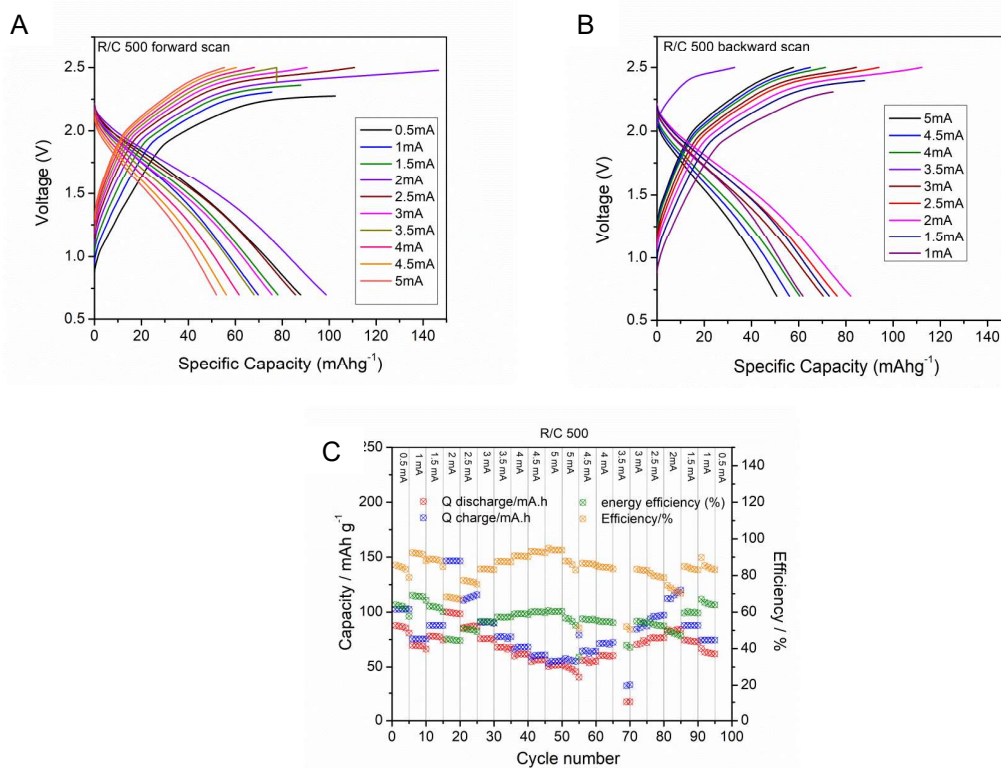


Figure 30: Discharge capacity evaluation of R/C₅₀₀; (A-B) Galvanostatic charge/discharge curve, (C) Rate capability curve

In figure 31 voltage curve of AIB cells with R/C₁₀₀₀ at different current density is given. We can see the overcharging of the cell at 2 mA current hence the coulombic efficiency dropped. Nevertheless, the discharge capacities are quite comparable with natural graphite. The system also shows good stability as the capacity has reduced from 79 to 74 mAhg⁻¹ while backward current scanning (from high to low current) at 1mA.

In figure 32 voltage profile of R/C₁₅₀₀ at various current rates is provided. R/C₁₅₀₀ shows 96 mAhg⁻¹ specific capacity at 0.5 mA current with 84% coulombic efficiency which is comparable with natural graphite. At higher current density the discharge capacity is very low (23 mAhg⁻¹) at 3 mA current with 98% coulombic efficiency. A huge drop in discharge capacities with higher current rate was observed, shows slow kinetics at cathode.

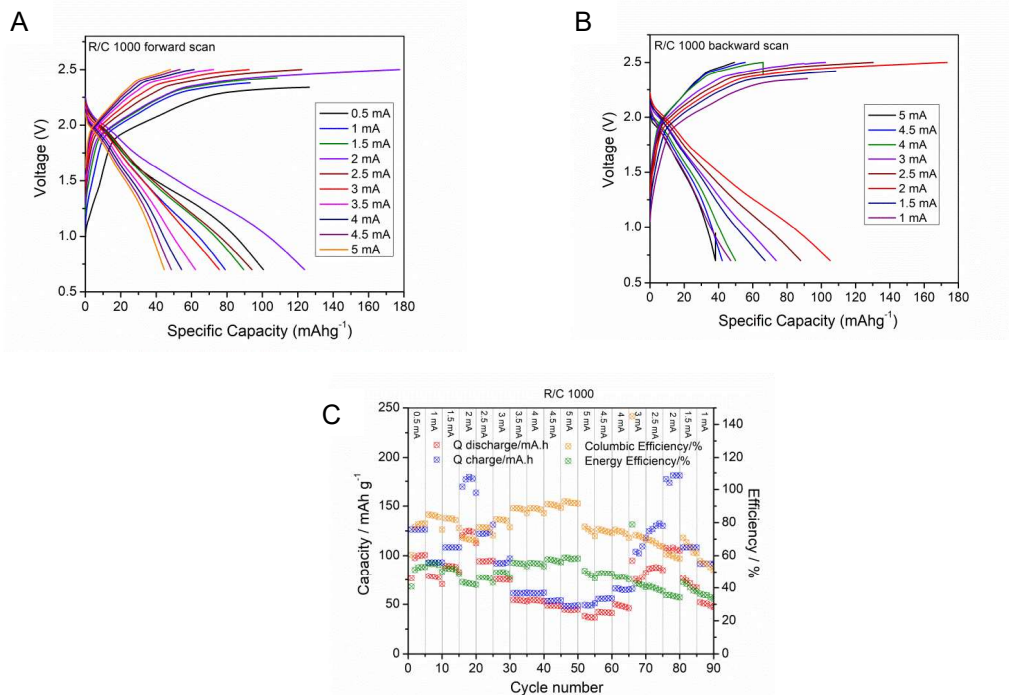


Figure 31: Discharge capacity evaluation of R/C₁₀₀₀; (A-B) Galvanostatic charge/discharge curve, (C) Rate capability curve

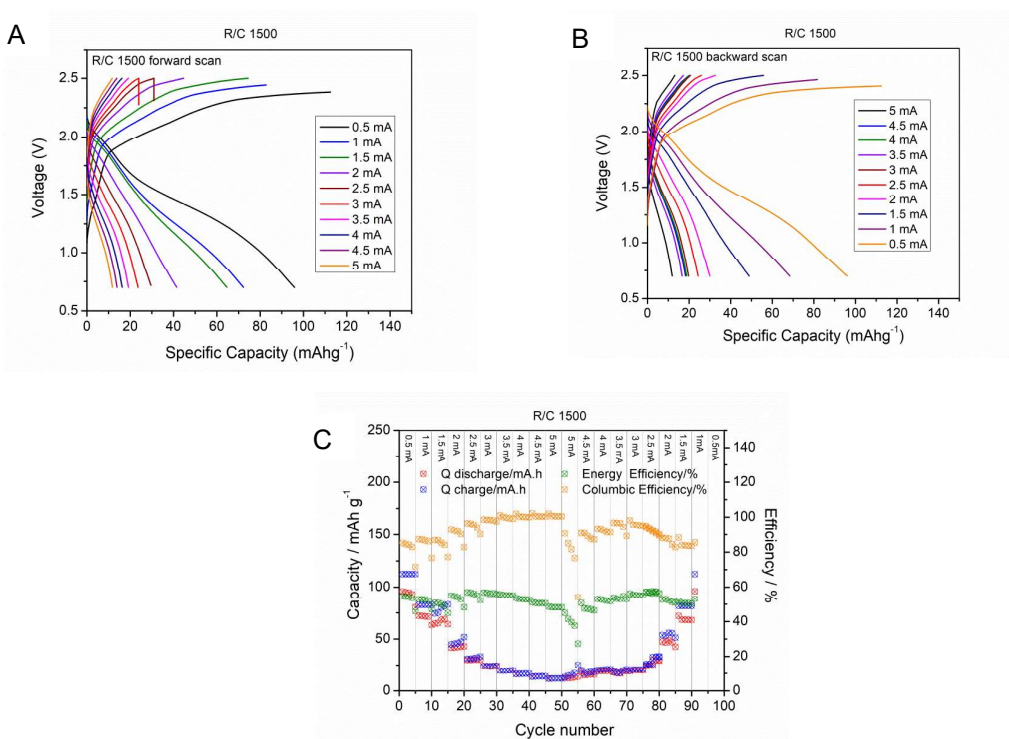


Figure 32: Discharge capacity evaluation of R/C₁₅₀₀; (A-B) Galvanostatic charge/discharge curve, (C) Rate capability curve

3.7.2.3. Discharge capacity evaluation of R/C₂₀₀₀, and R/C₂₅₀₀

Figure 33 and 34 shows the voltage curve of R/C₂₀₀₀ and R/C₂₅₀₀ at various current rates.

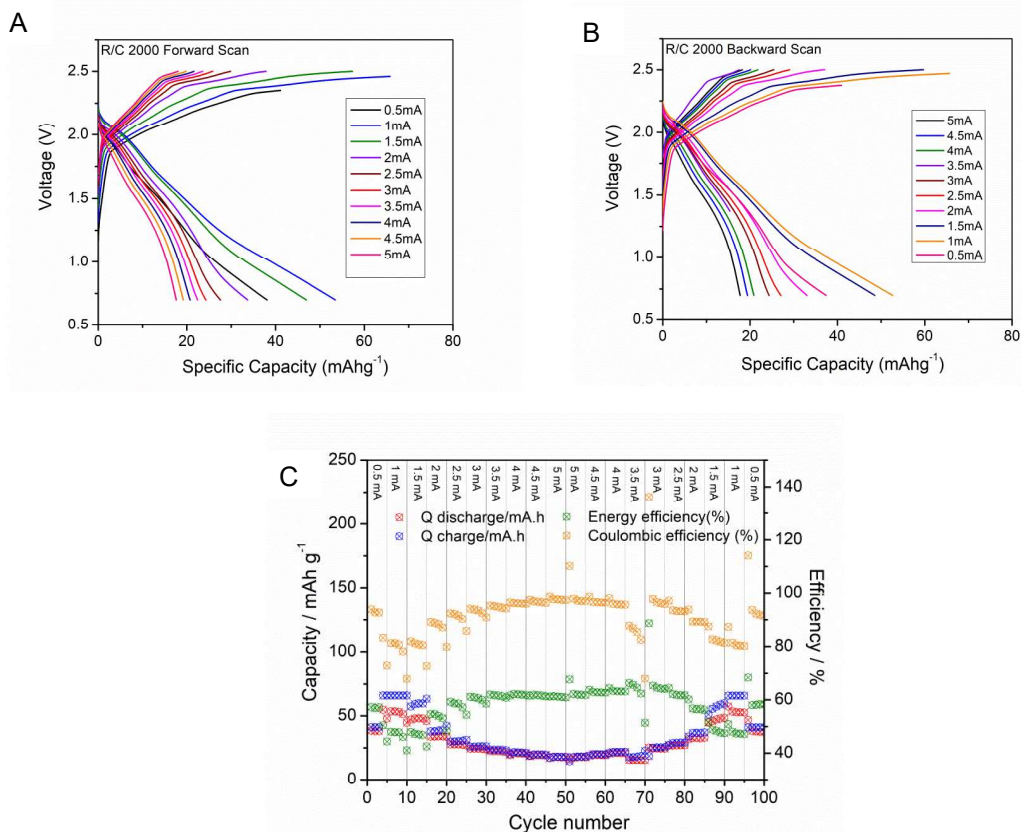


Figure 33: Discharge capacity evaluation of R/C₂₀₀₀; (A-B) Galvanostatic charge/discharge curve, (C) Rate capability curve

Discharge capacities in R/C₂₀₀₀ were detected 38 mAh/g, 53 mAh/g, 47 mAh/g, 34 mAh/g at 0.5mA, 1mA, 1.5mA, and 2mA current rate with 83%, 81%, 81%, and 88% coulombic efficiency respectively. In R/C₂₅₀₀, the discharge capacities were very low even at low current rate. At 0.5 mA current, the discharge capacity was obtained 36 mAhg⁻¹ with coulombic efficiency 70%. In both C_{XGs} (R/C₂₀₀₀ and R/C₂₅₀₀), the discharge capacity was found very less at high current rates.

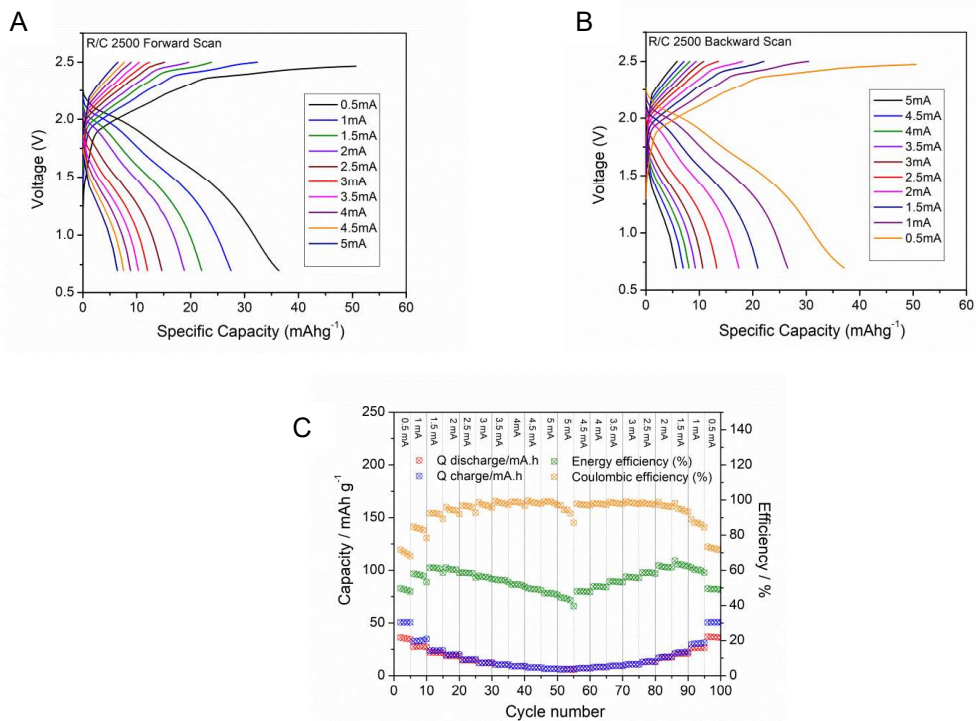


Figure 34: Discharge capacity evaluation of R/C₂₅₀₀; (A-B) Galvanostatic charge/discharge curve, (C) Rate capability curve

3.7.2.4. Discharge capacity evaluation of Natural Graphite (NG)

Natural graphite charge/discharge experiments are shown in figure 35 to compare C_{XG} with NG. It shows 92 mAhg⁻¹ discharge capacity with 98% coulombic efficiency. With higher current rates the discharge capacity gets lower to 79 mAhg⁻¹, 63 mAhg⁻¹, 54 mAhg⁻¹, 44 mAhg⁻¹, 32 mAhg⁻¹, 30 mAhg⁻¹, 20 mAhg⁻¹, 18 mAhg⁻¹, and 10 mAhg⁻¹ with 1 mA, 1.5 mA, 2 mA, 2.5 mA, 3 mA, 3.5 mA, 4 mA, 4.5 mA and 5 mA respectively with almost 98% - 100% coulombic efficiency. In addition, the NG system shows good stability which is clear with identical forward and backward scan rate capability curve.

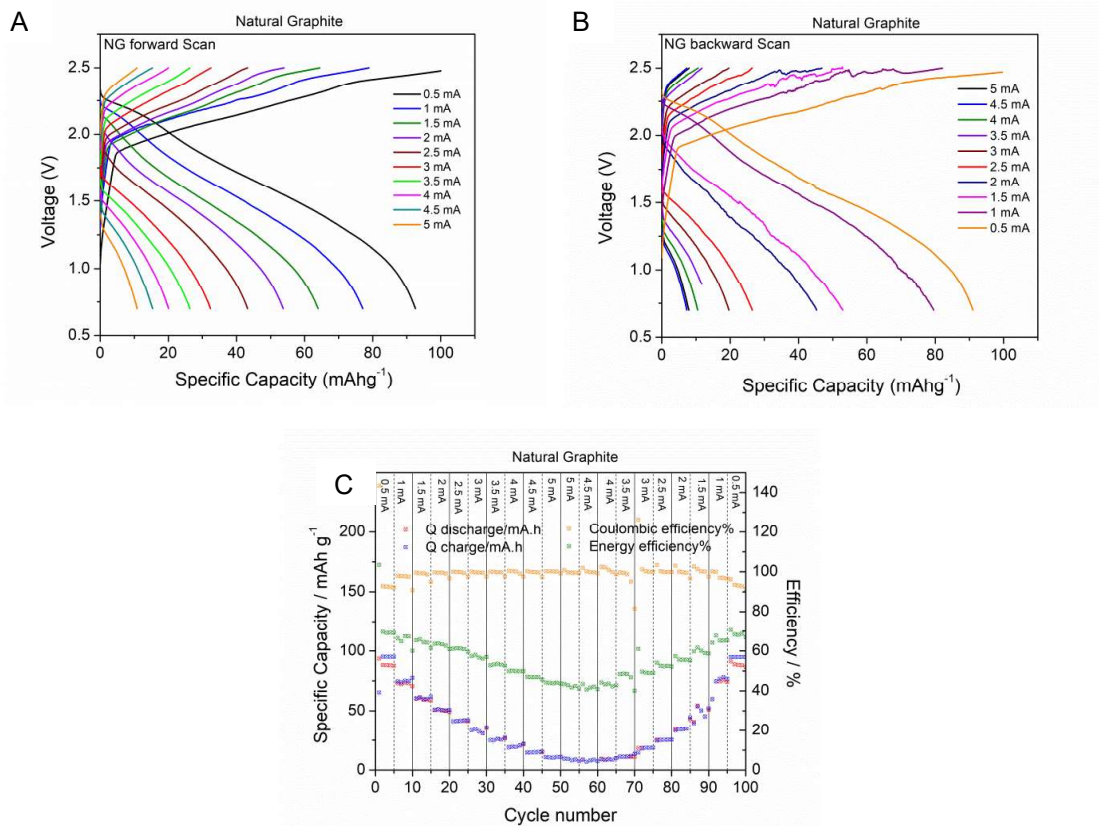


Figure 35: Discharge capacity evaluation of NG; (A-B) Galvanostatic charge/discharge curve, (C) Rate capability curve

From above results it is proved that R/C₅₀₀, R/C₁₀₀₀, and R/C₁₅₀₀ shows great discharge capacities which are comparable with NG. The reason for high discharge capacity of AIB cells with R/C₅₀₀, R/C₁₀₀₀ and R/C₁₅₀₀ could be the pore size. We assume that R/C₅₀₀, R/C₁₀₀₀, and R/C₁₅₀₀ has optimal pore size distribution to allow more facile intercalation/deintercalation of AlCl₄⁻ anion than carbon R/C₅₀, R/C₂₀₀₀ and R/C₂₅₀₀. In figure 36, galvanostatic charge/discharge curve was shown for R/C₅₀₀, R/C₁₀₀₀, R/C₁₅₀₀ in comparison with NG at 1 mA current and table 7 helps to compare specific discharge capacity of R/C₅₀₀, R/C₁₀₀₀, R/C₁₅₀₀ with NG.

Table 7: capacity comparison of AIB cells with C_{XG} R/C₅₀₀, 1000 and 1500 with NG at 1 mA

Sample	Current mA	Discharge Capacity mAh/g	Coulombic Efficiency %
R/C ₅₀₀	1	70	92
R/C ₁₀₀₀	1	79	84
R/C ₁₅₀₀	1	65	79
NG	1	77	97

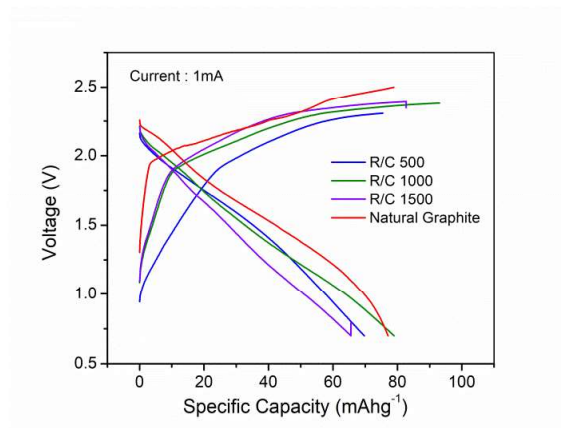
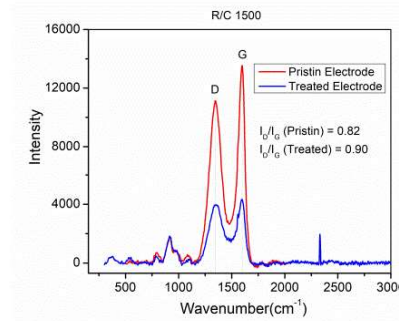
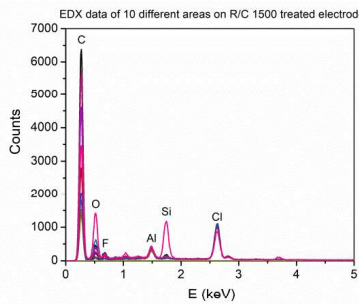
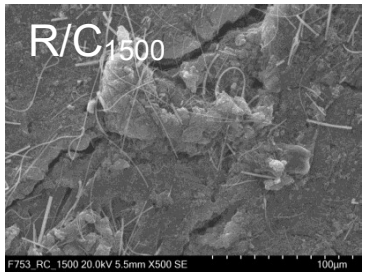
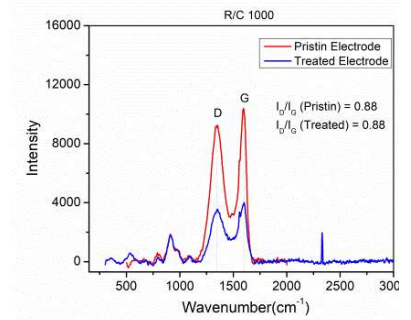
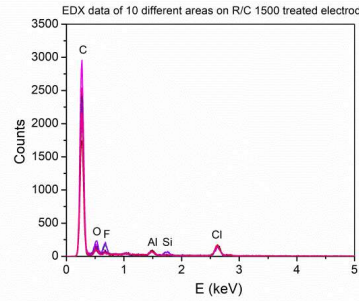
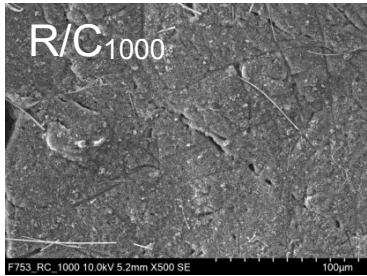
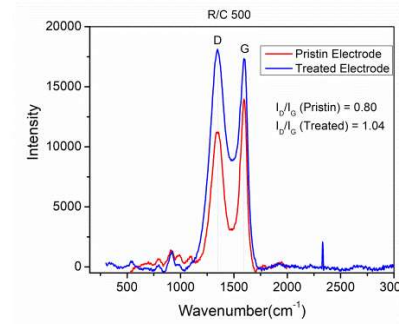
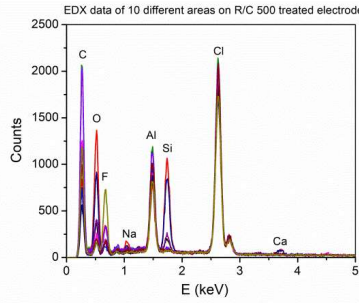
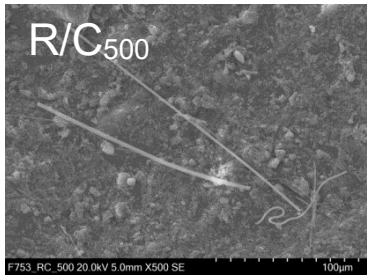
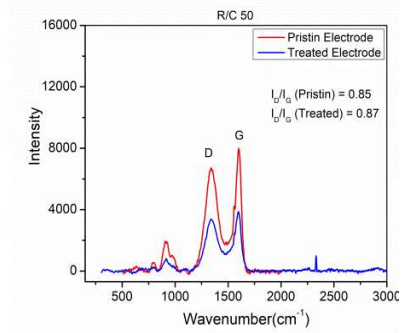
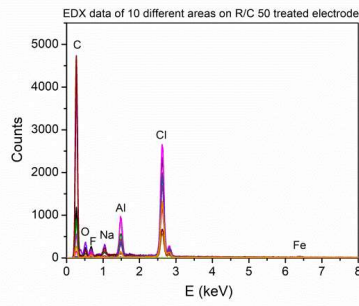
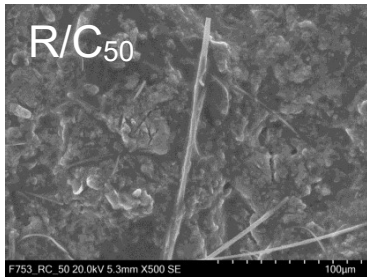


Figure 36: Galvanostatic charge/discharge curve of Al cells with C_{XG} R/C₅₀₀, R/C₁₀₀₀, R/C₁₅₀₀ and NG at 1mA current value

3.8. Post-mortem study of C_{XG} cathode electrochemical tests

Post mortem study of carbon C_{XGs} after electrochemical measurements was done with the help of Energy-dispersive X-ray spectroscopy (EDX) and Raman spectroscopy. EDX data of R/C₅₀, R/C₅₀₀, R/C₁₀₀₀, R/C₁₅₀₀, R/C₂₀₀₀, and R/C₂₅₀₀ is displayed in figure 37 along with their SEM images and Raman measurements (after electrochemical measurements). These studies helped us to find out the elemental composition of C_{XG} and structural changes occurred during or after electrochemical measurements.



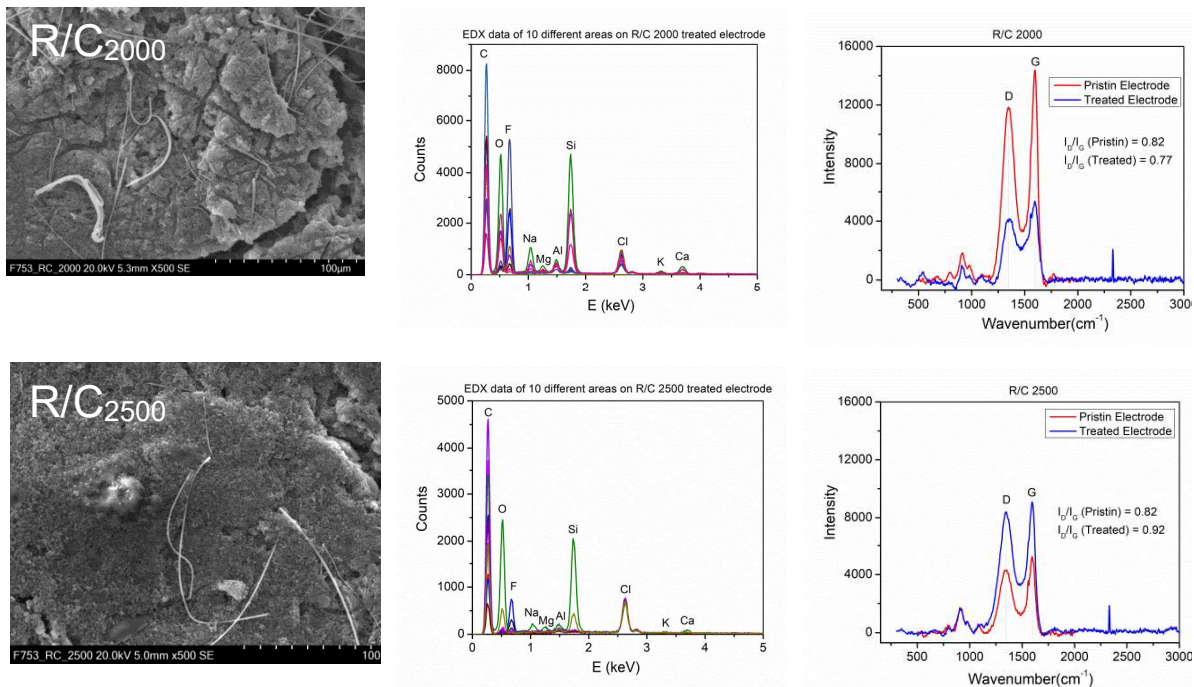


Figure 37: Post-mortem study of C_{xG_s} with SEM images of carbon C_{xG_s} , EDX and Raman spectra
 A) R/C₅₀ B) R/C₅₀₀ C) R/C₁₅₀₀ D) R/C₂₀₀₀

EDX spectra show an intense carbon peak in all samples which is associated to the carbon of C_{xG_s} . In most of samples Al and Cl peaks are presented in 1:3 (atomic%) ratio with oxygen which indicates the presence of $AlCl_3$ molecule and in some C_{xG_s} ratio of Al and Cl is 1:4 which. Moreover, in all electrochemically treated C_{xG_s} , fiber like structure is present that belongs to the glass fiber separator that has been used in EL cell during experiment. High Si amount in EDX curve is because of these glass fibers. Oxygen is also a common element in all EDX graphs which is because of uncarbonized ether bond present in non-pyrolyzed C_{xG} may be because of $Al(OH)_3$ species which generates when $AlCl_3$ reacts with water. Since polytetrafluoroethylene (PTFE) binder was used during ink preparation of cathode hence there is a common fluorine (F) peak in all EDX spectra. In R/C₅₀₀, R/C₂₀₀₀ and R/C₂₅₀₀ electrodes there are few low intensity peaks that belong to Na, Mg, Ca, K and also Fe in R/C₅₀. Presence of Fe peaks is due to corrosive nature of electrolyte that leads the corrosion of EL cell made up of stainless steel.

Raman spectra of treated electrodes were compared with pristine one in figure 37. I_D/I_G in pristine electrode was found to be lower than that of aged cathodes. Moreover, in carbon xerogel R/C₅₀₀, D band shows higher intensity than G band.

These observations may be an indication for increasing in defects due to C bond rupture during intercalation and de-intercalation steps. In the conclusion we can say that intercalation and de-intercalation processes during measurements has formed deflection in C_{XG} structure hence the intensity of D band has increased than pristine. R/C_{500} shows very high degree of deflection shows I_D/I_G more than one. The peak shifting between pristine and treated cathode is negligible hence the energy of the system has not changed.

Table 8: I_D & I_G values comparison between pristine and treated electrode

Sample	pristine cathode			treated cathode		
	I_D	I_G	I_D/I_G	I_D	I_G	I_D/I_G
R/C₅₀	6675	7990	0.85	3367	3865	0.87
R/C₅₀₀	11225	13945	0.80	18109	17339	1.04
R/C₁₀₀₀	9245	10381	0.88	3561	4011	0.88
R/C₁₅₀₀	11135	13547	0.82	3955	4334	0.90
R/C₂₀₀₀	11852	14373	0.82	4166	5363	0.77
R/C₂₅₀₀	4291	5234	0.82	8399	9096	0.92

From Table 8 it can be seen that for R/C_{500} and R/C_{2500} after cycling the intensities of D and G-band were significantly higher than for pristine cathodes. The reason for this observation is actually not clear but we suppose two possibilities: the first one might be related to the focus of the instrument. The focus has a big influence on the measured intensity. If the sample is slightly out of focus the measured intensity will be less than in focus. The other possibility is related to the sample. It might be possible that due to the cycling operation the morphology of the sample has changed.

4. CONCLUSION AND OUTLOOK

Carbon C_{XGs} were successfully synthesized by facile and affordable method using resorcinol and formaldehyde as educts and sodium carbonate as catalyst. Raman and XRD data prove that C_{XGs} are amorphous in nature with high number of disordered carbon domains. From the analysis of BET data, it can be seen that R/C ratio controls the surface area and porosity of C_{XGs} . Galvanostatic charge/discharge experiments prove R/C₅₀₀, R/C₁₀₀₀ and R/C₁₅₀₀ C_{XG} as effective cathode material with excellent discharge capacities which is comparable with natural graphite. R/C₅₀₀ shows 88 mAhg⁻¹ specific discharge capacity with 85% coulombic efficiency at 0.5 mA current. Even at high current (5mA) the discharge capacity amounted to 52 mAhg⁻¹ with 93% coulombic efficiency. On the other hand, R/C₁₀₀₀ and R/C₁₅₀₀ show 101 mAhg⁻¹ discharge capacity with 77% coulombic efficiency and 96 mAhg⁻¹ discharge capacity with 84% coulombic efficiency, respectively. However, at high current (5mA), R/C₁₅₀₀ hangs behind as it shows only 11 mAhg⁻¹ discharge capacity with 100% coulombic efficiency. A summary of the AIB performance at 1 mA is given in table 9. Best results in terms of capacity were yielded by AIB cells with R/C₅₀₀ & R/C₁₀₀₀ followed by R/C₁₅₀₀.

Table 9: Summary of discharge capacity & coulombic efficiency of AIB performance with different C_{XG} cathode materials at 1 mA current value (backward scan) as well as one cell with NG as reference

Sample	Discharge Capacity mAhg ⁻¹	Coulombic Efficiency %
R/C ₅₀	52	68
R/C ₅₀₀	70	92
R/C ₁₀₀₀	79	84
R/C ₁₅₀₀	65	79
R/C ₂₀₀₀	53	81
R/C ₂₅₀₀	28	85
NG	77	97

This work not only demonstrates a great impetus of utilization carbon C_{XGs} as cathode material in Al ion battery but also gives an easy synthesis route to synthesize carbon C_{XG} with tunable pore sizes.

Following experiments have to be carried out to complete investigation of more promising carbon xerogels samples:

- 1) Systematic investigation of pore size distribution
- 2) Conductivity measurements
- 3) TGA experiment in air for thermal stability
- 4) Long term charge/discharge cycling tests of AIB cell

REFERENCES

1. Winter, M. & Brodd, R. J. What are batteries, fuel cells, and supercapacitors? *Chem. Rev.* **104**, 4245–4269 (2004).
2. Deng, D. Li-ion batteries: Basics, progress, and challenges. *Energy Sci. Eng.* **3**, 385–418 (2015).
3. Endo, A., Miyake, M. & Hirato, T. Electrodeposition of Aluminum from 1,3-Dimethyl-2-Imidazolidinone/AlCl₃ baths. *Electrochim. Acta* **137**, 470–475 (2014).
4. Holland, A., Mckerracher, R. D., Cruden, A. & Wills, R. G. A. An aluminium battery operating with an aqueous electrolyte. *J. Appl. Electrochem.* **48**, 243–250 (2018).
5. Kitada, A., Nakamura, K., Fukami, K. & Murase, K. Electrochemically active species in aluminum electrodeposition baths of AlCl₃/glyme solutions. *Electrochim. Acta* **211**, 561–567 (2016).
6. Ye, D., Luo, B., Max Lu, G. & Wang, L. Will new aluminum-ion battery be a game changer? *Sci. Bull.* **60**, 1042–1044 (2015).
7. Lin, M.-C. *et al.* An ultrafast rechargeable aluminium-ion battery. *Nature* **520**, 324 (2015).
8. Job, N. *et al.* Carbon aerogels, cryogels and xerogels: Influence of the drying method on the textural properties of porous carbon materials. *Carbon N. Y.* **43**, 2481–2494 (2005).
9. Pekala, R. W. Organic aerogels from the polycondensation of resorcinol with formaldehyde. *J. Mater. Sci.* **24**, 3221–3227 (1989).
10. Lin, C. & Ritter, J. A. Effect of synthesis PH on the structure of carbon xerogels. *Carbon N. Y.* **35**, 1271–1278 (1997).
11. Canal-Rodríguez, M. Carbon Xerogels: The Bespoke Nanoporous Carbons. in (ed. Menéndez, J. A.) Ch. 3 (IntechOpen, 2018). doi:10.5772/intechopen.71255
12. Elia, G. A., Kyremateng, N. A., Marquardt, K. & Hahn, R. An Aluminum/Graphite Battery with Ultra-High Rate Capability. *Batter. Supercaps* (2018). doi:10.1002/batt.201800114
13. Job, N., Pirard, R., Marien, J. & Pirard, J.-P. Porous carbon xerogels with texture tailored by pH control during sol–gel process. *Carbon N. Y.* **42**, 619–628 (2004).

14. IKA®. Mixing and Processing Technology. (2015).
15. Gmbh, E. User Manual ECC-Ref Release 2.5. (2017).
16. Finkelstein, D. M., Schumacker, R. E. & Lomax, R. G. A Beginner's Guide to Thermogravimetric Analysis. *Technometrics* **47**, 522–522 (2005).
17. Inkson, B. J. *Scanning Electron Microscopy (SEM) and Transmission Electron Microscopy (TEM) for Materials Characterization. Materials Characterization Using Nondestructive Evaluation (NDE) Methods* (Elsevier Ltd, 2016). doi:10.1016/B978-0-08-100040-3.00002-X
18. Harris, J. R. & Adrian, M. Preparation of thin-film frozen-hydrated/vitrified biological specimens for cryoelectron microscopy. *Methods Mol. Biol.* **117**, 31–48 (1999).
19. Zhou, W., Apkarian, R., Wang, Z. L. & Joy, D. Fundamentals of scanning electron microscopy (SEM). *Scanning Microsc. Nanotechnol. Tech. Appl.* 1–40 (2007). doi:10.1007/978-0-387-39620-0_1
20. Liao, Y. *Practical Electron Microscopy and Database: www.globalsino.com/EM/*. (2013).
21. Fisher, R. M., Szirmai, A., Bain, E. C. & Mclear, J. H. Electron Microscopy. *Anal. Chem.* **42**, 362–366 (1970).
22. Kirkpatrick, R. J. *Handbook of Analytical Techniques in Concrete Science and Technology. Handbook of Analytical Techniques in Concrete Science and Technology* (2001). doi:10.1016/B978-081551437-4.50009-6
23. Bunaciu, A. A., Udriștioiu, E. gabriela & Aboul-Enein, H. Y. X-Ray Diffraction: Instrumentation and Applications. *Crit. Rev. Anal. Chem.* **45**, 289–299 (2015).
24. Bumbrah, G. S. & Sharma, R. M. Raman spectroscopy – Basic principle, instrumentation and selected applications for the characterization of drugs of abuse. *Egypt. J. Forensic Sci.* **6**, 209–215 (2016).
25. Moura, C. C., Tare, R. S., Oreffo, R. O. C. & Mahajan, S. Raman spectroscopy and coherent anti-Stokes Raman scattering imaging: Prospective tools for monitoring skeletal cells and skeletal regeneration. *J. R. Soc. Interface* **13**, 9–11 (2016).
26. Elgrishi, N. *et al.* A Practical Beginner's Guide to Cyclic Voltammetry. *J. Chem. Educ.* **95**, 197–206 (2018).
27. Vicentini, R. *et al.* How to measure and calculate equivalent series resistance of electric double-layer capacitors. *Molecules* **24**, (2019).
28. Job, N., Sabatier, F., Pirard, J. P., Crine, M. & Léonard, A. Towards the

- production of carbon xerogel monoliths by optimizing convective drying conditions. *Carbon N. Y.* **44**, 2534–2542 (2006).
29. Oyedoh, E. A., Albadarin, A. B., Walker, G. M., Mirzaeian, M. & Ahmad, M. N. M. Preparation of controlled porosity resorcinol formaldehyde xerogels for adsorption applications. *Chem. Eng. Trans.* **32**, 1651–1656 (2013).
 30. Childres, I., Jauregui, L. A., Park, W., Caoa, H. & Chena, Y. P. Raman spectroscopy of graphene and related materials. *New Dev. Phot. Mater. Res.* 403–418 (2013).
 31. Horikawa, T., Hayashi, J. & Muroyama, K. Controllability of pore characteristics of resorcinol-formaldehyde carbon aerogel. *Carbon N. Y.* **42**, 1625–1633 (2004).